

From typhoon rainfall to slope failure: optimizing susceptibility models and dynamic thresholds for landslide warnings in Zixing City, China

Weifeng Xiao¹, Guangchong Yao¹, Zhenghui Xiao¹, Ge Liu^{*2}, Luguang Luo¹, Yunjiang Cao¹, Wei Yin³

¹School of Earth Sciences and Spatial Information Engineering, Hunan University of Science and Technology, Xiangtan 411201, China

²Northeast Institute of Geography and Agroecology, CAS, Changchun 130102, China

³Hunan Institute of Geological Disaster Investigation and Monitoring, Changsha 410004, China

Corresponding author.

E-mail address: liuge@iga.ac.cn (Ge Liu)

Abstract: Typhoon-specific rainfall-induced landslides present a severe threat in mountainous regions. Existing warning systems, however, often fail to account for the distinct rainfall dynamics of these extreme events. To bridge this gap, an integrated framework is proposed, combining optimized susceptibility predictions with dynamic rainfall thresholds tailored to typhoon patterns. The approach enhances machine learning accuracy through buffer-based negative sampling and variable weighting. It also introduces a spatiotemporal rainfall analysis to distinguish between short-term intense downpours and cumulative soil saturation. Tested in Zixing City, Hunan Province, China, following over 700 landslides triggered by Typhoon Gaemi, the framework proved its effectiveness. Support Vector Machine (SVM) models with frequency ratio (FR) inputs yielded the highest accuracy in predicting these slope failures. Rainfall analysis identified the combination of 24-hour intensity and 7-day antecedent rainfall as the optimal trigger. This pairing effectively captures both immediate and cumulative moisture effects. Spatially, granite slopes and areas near roads emerged as critical hotspots for failure. Ultimately, the framework generates high-risk zone

28 maps that align strongly with historical events. This work underscores the unique nature of
29 typhoon-driven slope instability and offers a transferable framework for disaster risk
30 reduction in cyclone-prone regions.

31 **Keywords:** Typhoon-induced landslide; Slope failure; Hazard warning system; Dynamic
32 thresholds; Landslide susceptibility mapping

33 1 Introduction

34 Landslides pose significant threats to mountainous regions globally (Froude and Petley,
35 2018), especially in areas where steep terrain, complex geology (Thiene et al., 2017), and
36 extreme weather events like typhoons intersect. In Southeast China, typhoon-induced
37 landslides have become a growing concern due to the region's rapid urbanization and the
38 increasing variability in climate patterns (Gariano and Guzzetti, 2016; Fan et al., 2018). The
39 Nanling Mountains, in southern China, are particularly vulnerable to landslides due to a
40 combination of extreme topographic relief and complex geological conditions during the
41 typhoon season (Zou et al., 2023).

42 Typhoons typically bring prolonged antecedent rainfall, followed by intense, short bursts
43 of precipitation (Li et al., 2019). These conditions create unique hydrological environments
44 that exceed the complexity of typical rainfall-triggered landslides (Chung and Li, 2022).
45 These events trigger slope failures through cumulative soil saturation and sudden hydrological
46 stress, challenging traditional landslide prediction methods (Yang et al., 2017). Despite
47 advances in landslide susceptibility prediction (LSP) and rainfall threshold modeling, current
48 approaches remain inadequate. Three critical limitations persist: severe data imbalance effects,
49 suboptimal integration of variable selection with machine learning algorithms, and lack of
50 spatially-explicit rainfall thresholds for typhoon-specific conditions (Segoni et al., 2018a;
51 Regmi et al., 2024).

删除[肖巍峰]: From typhoon rainfall to slope failure, this study addresses the urgent need for typhoon-adapted hazard warning systems in mountainous regions like Zixing City, China. We develop an integrated framework to optimize dynamic susceptibility models and rainfall thresholds by leveraging machine learning (ML) and spatiotemporal rainfall analysis. Using buffer-based negative sampling (0.1–5.0 km) and variable weighting methods (information value (IV), certainty factor (CF), and frequency ratio (FR)), we compare two ML models: Support Vector Machine (SVM) and Light Gradient Boosting Machine (LightGBM). The SVM model with FR input at 0.5 km buffer achieved the highest accuracy (AUC=0.913), correctly classifying 86.4% of landslides in high-risk zones, revealing how typhoon-driven hydrology interacts with slope instability. For rainfall thresholds, the H24-D7 model (24-hour intensity vs. 7-day antecedent rainfall) emerged as optimal (71.8% accuracy), effectively capturing typhoon-specific triggers like short-term downpours and cumulative soil saturation. Kriging interpolation generated spatially explicit thresholds, identifying granite slopes and road-proximal areas as hotspots for typhoon-induced failures. The final hazard warning system, integrating susceptibility and dynamic thresholds, showed 71.4% overlap with historical landslides, emphasizing the critical role of typhoon rainfall dynamics in slope failure prediction. This work provides a scalable approach for regions facing typhoon-related landslide risks, prioritizing both spatial heterogeneity and temporal rainfall patterns

52 Most existing studies employ ad-hoc buffer distances without systematic optimization,
53 leading to inconsistent model performance across different geological settings (Lombardo and
54 Mai, 2018). Traditional methods attempt to mitigate this imbalance by randomly sampling
55 non-landslide points across the study area (Steger et al., 2016; Dou et al., 2023). However,
56 random selection can introduce spatial bias, as non-landslide points might include areas that
57 are unstable but have not yet been identified as landslide-prone (Kalantar et al., 2018).

58 To address this limitation, more recent approaches have employed buffer-based negative
59 sampling, which systematically excludes non-landslide points near known landslide sites.
60 This method assumes that adjacent areas share similar environmental conditions (e.g., slope,
61 lithology) and therefore should not be classified as “stable” (Achu et al., 2022). Several
62 studies have tested varying buffer distances, ranging from tens to thousands of meters, to
63 determine the optimal distance for different regions. However, systematic evaluation of buffer
64 distance optimization coupled with variable weighting methods remains largely unexplored.

65 LSP is primarily focused on identifying areas prone to slope failure, based on static
66 environmental factors such as topography, lithology, land cover, and hydrology (Zézere et al.,
67 2017; Guo et al., 2024). Traditional approaches to LSP often rely on deterministic and
68 statistical methods, including information value (IV), certainty factor (CF), frequency ratio
69 (FR), logistic regression (LR), and weight of evidence (WOE). These methods quantify the
70 relationship between historical landslide occurrences and predisposing factors using linear or
71 semi-linear approaches (Ciurleo et al., 2017; Reichenbach et al., 2018). However, these
72 methods oversimplify the complex, nonlinear interactions that govern slope stability
73 (Merghadi et al., 2020).

74 In contrast, machine learning (ML) algorithms, such as support vector machine (SVM)
75 and light gradient boosting machine (LightGBM), have emerged as powerful alternatives.
76 SVM excels in high-dimensional classification tasks and effectively identifies optimal

77 hyperplanes separating landslide-prone from stable areas (San, 2014; Huang and Zhao, 2018).
78 LightGBM offers superior scalability and computational efficiency for processing large
79 geospatial datasets (Sun et al., 2023). Both SVM and LightGBM capture intricate
80 relationships among variables without restrictive assumptions, making them superior to
81 traditional methods in terms of predictive accuracy (Yang et al., 2023). However, frameworks
82 that systematically integrates variable weighting methods with advanced ML algorithms for
83 LSP optimization are lacking.

84 For temporal prediction, existing rainfall threshold approaches predominantly use
85 generalized regional thresholds that inadequately capture local geological heterogeneity and
86 typhoon-specific rainfall patterns (Guzzetti, 2021; Banfi and De Michele, 2024). These
87 thresholds are typically defined based on cumulative or intensity-duration (I-D) rainfall values
88 (Piciullo et al., 2017; Segoni et al., 2018a). In typhoon-prone regions, dynamic rainfall
89 thresholds are crucial due to the unique combination of long-duration antecedent rainfall and
90 sudden high-intensity bursts of precipitation (Guzzetti et al., 2020). Traditional empirical
91 methods fail to provide spatially continuous threshold surfaces that account for local
92 environmental variability (Piciullo et al., 2018).

93 Recent advances have integrated multi-temporal rainfall parameters with advanced
94 statistical techniques to optimize rainfall thresholds (Segoni et al., 2015; Huang et al., 2022),
95 accounting for diverse triggering mechanisms. Additionally, spatial interpolation methods,
96 such as Kriging, have been applied to generate continuous rainfall threshold surfaces that
97 allow for local variations in geological and environmental conditions (Kenanoglu et al., 2019;
98 Segoni et al., 2018b). This approach, when combined with high-resolution susceptibility maps,
99 contributes to the development of integrated hazard warning systems that can dynamically
100 adjust to typhoon-specific rainfall-induced scenarios (Piciullo et al., 2018; Mirus et al., 2018).

101 This study examines Zixing City, a mountainous region in southeastern Hunan Province,
102 frequently affected by typhoon-induced extreme rainfall. Its steep slopes, fractured geology,
103 and high sensitivity to rapid pore-pressure increase render it particularly vulnerable (Ma et al.,
104 2025). The large number of landslides (>700) triggered by Typhoon Gaemi in July 2024
105 provides a valuable dataset for model calibration and validation.

106 Here we developed an integrated framework that combines (i) optimised buffer distances
107 for negative sampling, (ii) bivariate weighting methods (IV, CF, FR) with advanced machine
108 learning classifiers (SVM, LightGBM), and (iii) spatially continuous, typhoon-specific
109 rainfall thresholds derived through Kriging interpolation. The specific objectives are to (1)
110 determine optimal buffer distances that minimise spatial bias in imbalanced datasets, (2)
111 evaluate the performance gain from coupling bivariate weights with machine learning
112 algorithms, (3) establish dynamic rainfall thresholds suited to typhoon rainfall patterns, (4)
113 generate continuous threshold surfaces via Kriging, and (5) integrate high-resolution
114 susceptibility maps with these thresholds to support an operational early warning system. This
115 approach improves landslide prediction in typhoon-prone mountainous regions and provides a
116 transferable methodology for similar environments.

117 2 Study area and data sources

118 2.1 Study area

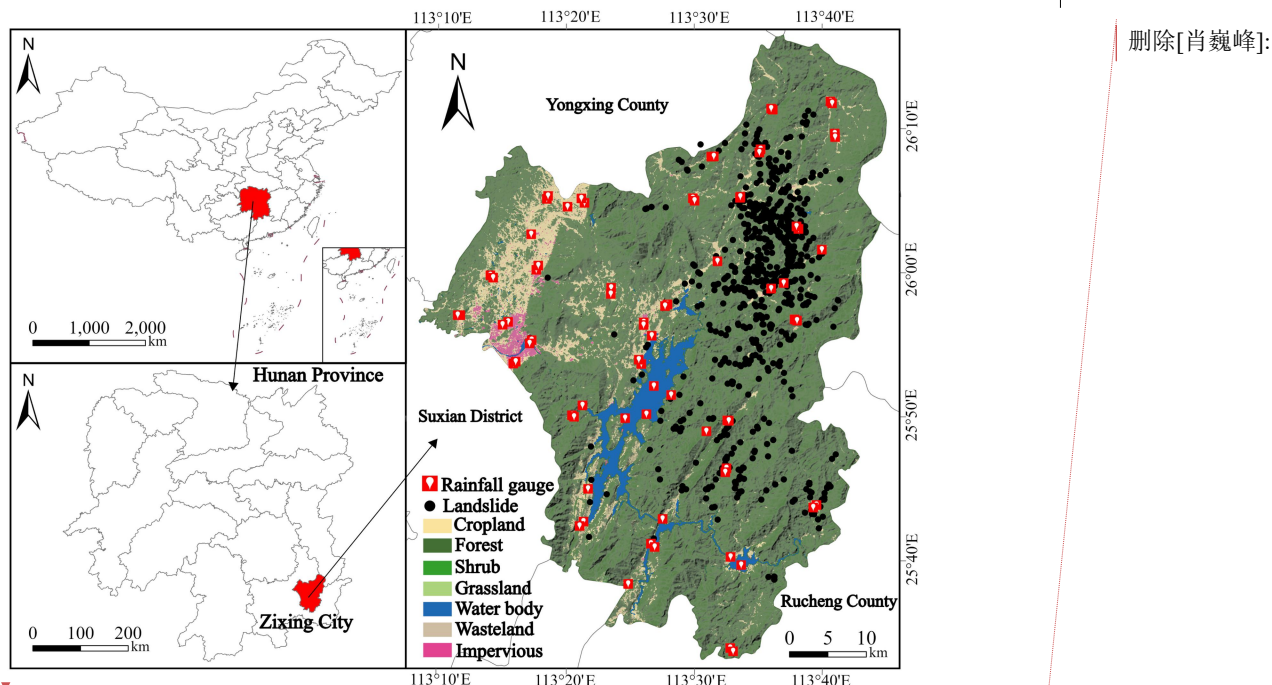
119
120 Zixing City (25°34'–26°18' N, 113°08'–113°44' E), covering 2,747 km² in southeastern
121 Hunan Province, China (Fig. 1), is located within the Nanling Mountains geological province.
122 Situated approximately 400 km inland from the South China Sea, Zixing lies at the
123 intersection of the Nanling Mountains and low hills, forming a watershed divide between the
124 Yangtze and Pearl River basins. The region is characterized by steep topography, with
125 elevations ranging from 125 to 1,691 meters and slopes exceeding 30° across 78% of the area.

删除[肖巍峰]: Landslides are among the most devastating natural hazards, particularly in regions with steep terrain, complex geology, and high rainfall variability (Thiene et al., 2017; Froude and Petley, 2018). As rapid urbanization and climate change exacerbate the frequency of typhoon-induc ...

删除[肖巍峰]: Zixing City, situated in southeastern Hunan Province, China (25°34'–26°18' N, 113°08'–113°44' E), spans 2,746 km² and is characterized by rugged topography, with over 200 peaks exceeding 800 meters in elevation (Fig. 1). As a typhoon-prone mountainous region in southern Hunan, it ...

126 This mountainous terrain, combined with fractured geology and active NE-SW trending faults
127 such as the Chaling-Yongxing Fault Zone, creates a permeable fracture network that
128 facilitates groundwater drainage.

129 The climate of Zixing is subtropical monsoon, with annual precipitation averaging 1,550
130 mm, 70% of which occurs from April to September. Typhoons significantly contribute to
131 rainfall, inducing rapid pore-pressure increases in shallow aquifers (3–8 m depth). These
132 climatic and geological conditions make Zixing particularly vulnerable to landslides,
133 providing a valuable context for this study. The extensive landslide dataset triggered by
134 Typhoon Gaemi in July 2024 (>700 events) serves as a critical resource for model calibration
135 and validation.



137 **Figure 1.** Geographical distribution of the study area, landslides and rainfall gauges.

138 **2.2 Data collection and preprocessing**

139 **2.2.1 Compilation of landslide catalogue**

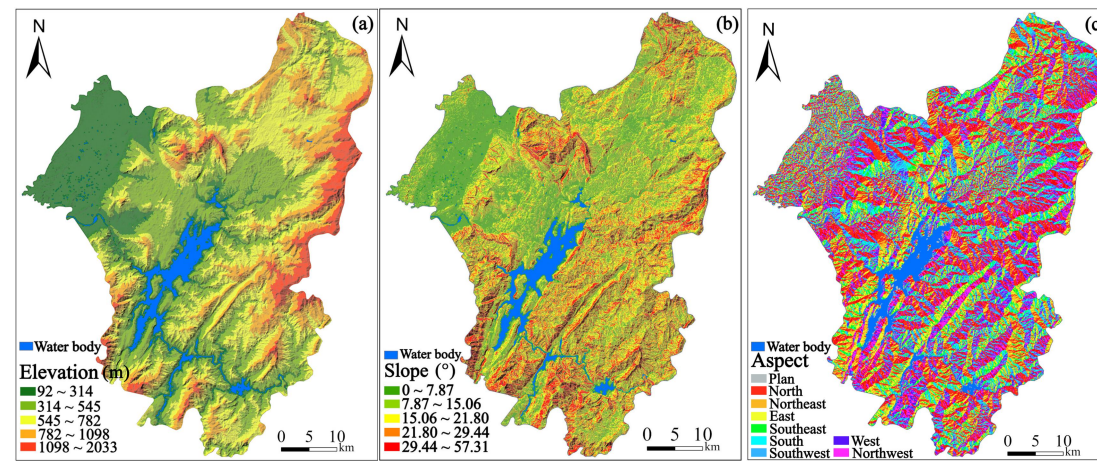
140 A comprehensive inventory of 705 landslide events triggered by Typhoon Gaemi on July
141 27, 2024, was compiled from the Hunan Center for Natural Resources Affairs. The landslide

142 locations were verified through field inspections and high-resolution satellite imagery to
143 ensure spatial accuracy and completeness of the dataset.

144 **2.2.2 Landslides-related conditioning factors and data sources**

145 Based on extensive literature reviews and the geoenvironmental characteristics of the
146 study area, twelve conditioning factors were selected for landslide susceptibility analysis:
147 elevation, slope gradient, slope orientation, curvature, topographic wetness index (TWI),
148 stream power index (SPI), normalized difference vegetation index (NDVI), distances to roads,
149 rivers, and faults, and lithology (Fig. 2).

150 Topographic factors (elevation, slope gradient, slope orientation, TWI, SPI, and
151 curvature) were extracted from a 30-meter digital elevation model (DEM) obtained from the
152 Geospatial Data Cloud (<https://www.gscloud.cn>). Environmental factors including NDVI and
153 proximity variables (distances to roads, rivers, and fault lines) were derived from 1:50,000-
154 scale cartographic maps and Landsat 8 OLI imagery from the same platform. Geological
155 composition and structural data were acquired from 1:100,000-scale geological maps.



删除[肖巍峰]: Constructing an accurate landslide catalogue is crucial for landslide susceptibility prediction (Reichenbach et al., 2018). In this study, a total of 705 landslide events triggered by Typhoon “Gemei” on July 27, 2024, were documented. The dataset was obtained from the Hunan Center for Natural Resources Affairs, verified through field inspections and satellite imagery to ensure accuracy.

删除[肖巍峰]: Identifying key conditioning factors is essential for delineating landslide-prone areas. Based on literature reviews and the study area’s geo-environmental characteristics, twelve factors were selected, including elevation, slope gradient, slope orientation, curvatures, topographic wetness index (TWI), distance to road, river, fault, normalized difference vegetation index (NDVI), stream power index (SPI), and lithology (Fig. 2).

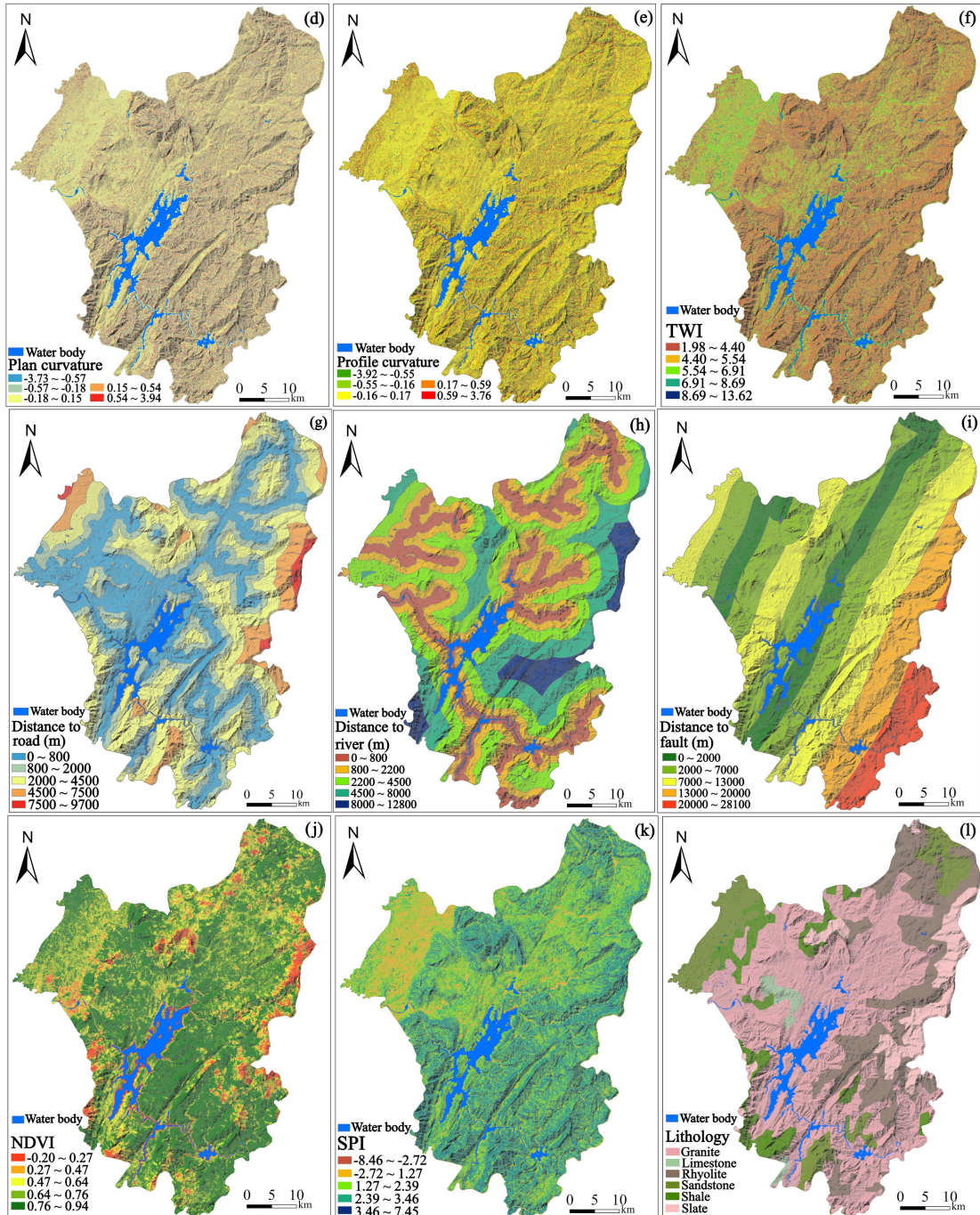


Figure 2. Landslide-related conditioning factors.

删除[肖巍峰]: Topographic factors, such as elevation, slope gradient, slope orientation, TWI, SPI, and curvature, were extracted from a 30-meter digital elevation model (DEM) sourced from the Geospatial Data Cloud (<https://www.gscloud.cn>). Environmental factors like NDVI, distances to roads, rivers, and fault lines were derived from 1:50,000-scale cartographic maps and Landsat 8 OLI imagery, both of which were also accessible via the Geospatial Data Cloud. Geological composition and fault line data were obtained from 1:100,000-scale geological maps. Hourly rainfall data from 12 meteorological stations during Typhoon "Gemei" were integrated to support dynamic threshold analysis.

For analysis, the study area was divided into 60×60 meter grid cells. Within this grid, 705 landslide events were recorded, each located within a unique grid cell and treated as positive samples for susceptibility analysis.

166 regional landslide analysis while maintaining compatibility with the available geological map
167 scale (1:100,000).

168 The study area was divided into 60×60 meter grid cells, with landslides smaller than the
169 grid resolution aggregated to the nearest cell centroid. Multiple landslides within a single cell
170 were treated as one event to maintain spatial independence required for machine learning
171 modeling. This preprocessing approach ensures statistical validity by minimizing spatial
172 autocorrelation effects while providing adequate representation of landslide distribution
173 patterns across the study area.

174 **2.2.4 Rainfall data collection and spatial distribution**

175 Rainfall data for the study were obtained from 12 automatic rain gauge stations
176 strategically distributed across Zixing City and its surrounding areas (Fig. 1). These stations,
177 operated by the Hunan Meteorological Administration, provided hourly precipitation records
178 during Typhoon Gaemi (July 20-30, 2024) and the preceding antecedent period. The spatial
179 distribution of gauge stations ensured adequate coverage of the study area's topographic and
180 climatic gradients.

181 To assign rainfall parameters (H1, H12, H24, H72, and D7) to each of the 705 landslide
182 points, we employed the Kriging interpolation to generate spatially continuous rainfall
183 surfaces from discrete gauge measurements. This geostatistical method accounts for spatial
184 autocorrelation in rainfall patterns and provides optimal unbiased estimates by weighting
185 nearby observations based on their spatial proximity and correlation structure.

186 Spherical variogram models were fitted to the rainfall data through iterative optimization,
187 with model selection based on minimum Akaike Information Criterion (AIC) values. The
188 interpolation accuracy was rigorously evaluated through leave-one-out cross-validation,
189 where each gauge station was sequentially removed and its rainfall values predicted using the
190 remaining 11 stations. Four statistical metrics were used to assess performance: Root Mean

191 Square Error (RMSE), Mean Absolute Error (MAE), correlation coefficient (R), and Nash-
192 Sutcliffe Efficiency (NSE).

193 **Table 1** Kriging interpolation accuracy assessment for rainfall parameters.

Parameter	RMSE (mm)	MAE	R	NSE
H1	4.2	3.1	0.76	0.71
H12	11.7	8.9	0.83	0.78
H24	16.3	12.6	0.87	0.82
H72	24.8	18.4	0.81	0.77
D7	29.6	22.7	0.78	0.73

194 The validation results demonstrated acceptable interpolation accuracy across all rainfall
195 parameters, with correlation coefficients ranging from 0.76 to 0.87 and Nash-Sutcliffe
196 Efficiency values between 0.71-0.82. Despite some limitations inherent to the sparse gauge
197 network in mountainous terrain, the interpolation performance was deemed sufficient for
198 regional landslide susceptibility analysis, ensuring reasonable spatial representation of
199 precipitation patterns across the study area.

200 3 Methodologies

201 This study proposes an integrated framework for optimizing landslide susceptibility
202 prediction (LSP) and typhoon-specific rainfall thresholds within hazard warning systems (Fig.
203 3). The framework includes the following key components: (1) landslide susceptibility
204 prediction and mapping, utilizing twelve conditioning factors prioritizing typhoon-induced
205 hydrological responses (e.g., TWI, SPI) and 705 landslide records from July 27, 2024,
206 optimized with five buffer distances and evaluated using ROC curves; (2) dynamic rainfall
207 threshold modeling based on typhoon rainfall parameterization, validated and spatially
208 interpolated using Kriging; and (3) the integration of spatial and temporal probabilities to
209 develop a typhoon-specific rainfall-induced landslide warning system, demonstrated through
210 a case study in Zixing City.

删除[肖巍峰]: typhoon-adapted hazard warning system,

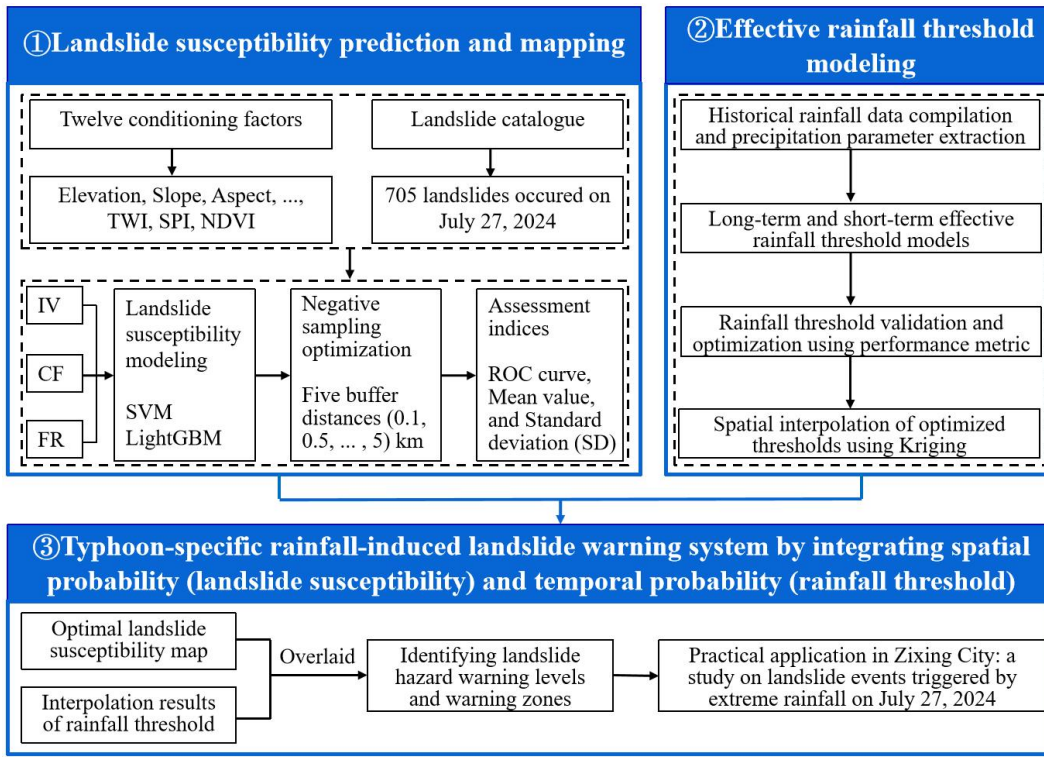


Figure 3. Technical framework for developing a [typhoon-specific rainfall-induced landslide warning system](#).

删除[肖巍峰]: typhoon rainfall-induced landslide hazard warning system

3.1 Landslide susceptibility prediction and mapping

3.1.1 Machine learning models

SVM is a robust supervised learning algorithm widely used for classification in landslide

susceptibility mapping (Kalantar et al., 2018; Wang et al., 2020). It operates by finding the optimal hyperplane that separates landslide-prone areas from stable regions in a multidimensional feature space. For typhoon-triggered landslides, SVM effectively handles imbalanced datasets caused by concentrated slope failures in high-intensity rainfall zones. The SVM optimization problem is defined as:

$$\min_{w,b,\xi} \frac{1}{2} w^T w + C \sum_{i=1}^n \xi_i \quad (1)$$

subject to the constraint:

$$y_i (w^T \phi(x_i) + b) \geq 1 - \xi_i, \quad \xi_i \geq 0, \quad i = 1, \dots, n \quad (2)$$

224 where w is the normal vector to the hyperplane, b is the bias term, ξ_i are slack variables, C is
225 the regularization parameter, and $\phi(x_i)$ maps input vectors to a higher-dimensional space. The
226 variable y_i represents the class label (-1 or 1) for each sample x_i .

227 LightGBM is an efficient gradient boosting framework for large datasets, known for
228 training an ensemble of decision trees by iteratively adding trees that minimize errors from
229 previous trees. LightGBM's scalability is critical for processing typhoon-related geospatial
230 data (e.g., hourly rainfall grids) across 2,746 km² (Sun et al., 2023; Sahin, 2020). The
231 minimized objective function is expressed as:

$$232 \quad L = \sum_{i=1}^N (y_i - \hat{y}_i)^2 + \lambda \sum_{j=1}^M \|\theta_j\|^2 \quad (3)$$

233 where y_i is the true label, \hat{y}_i is the predictive value, λ is a regularization parameter, and
234 θ_j represents the parameters of the model.

235 3.1.2 Input variable weighting methods

236 The IV method, grounded in information theory, assesses how different factors
237 contribute to landslide susceptibility within a study area (Niu et al., 2024). Factors such as
238 distance to roads and lithology were weighted higher in Zixing City due to their interaction
239 with typhoon-induced soil saturation. The IV for each evaluation factor is determined using
240 the formula below:

$$241 \quad IV(F_i, K) = \ln \frac{N_i / N}{S_i / S} \quad (4)$$

242 where $IV(F_i, K)$ is the information value of evaluation factor F_i in relation to landslide event K ,
243 N_i refers to the number of landslides, N is the total number of landslides, S_i represents the area
244 covered by factor F_i , and S is the total area of the study area.

245 The CF is a widely utilized probabilistic technique for assessing the likelihood of
246 landslide events (Zhao et al., 2021). It quantifies the prior probability of a landslide occurring

247 under various influential factor conditions using data from known landslide locations. The
248 expression of CF is as follows:

249

$$CF = \begin{cases} \frac{PP_a - PP_s}{PP_s(1-PP_a)}, & PP_a < PP_s \\ \frac{PP_a - PP_s}{PP_a(1-PP_s)}, & PP_a \geq PP_s \end{cases} \quad (5)$$

250 where CF is the certainty factor indicating the degree of association between an influential
251 factor and potential landslide occurrence. It is derived from two area-proportional measures:
252 PP_a , the proportion of landslide points within a specific factor class (number of landslide
253 points in the class / total area of the class); and PP_s , the proportion of landslide points across
254 the entire study region (total number of landslide points / total area of the region).

255 The FR is a prevalent method in statistical analysis that assesses the relative impact of
256 various factors on the incidence of landslides (Panchal et al., 2021). An elevated FR value
257 denotes a more significant influence of a factor on the likelihood of landslides. The FR is
258 determined by the following equation:

259

$$FR = \frac{N_i / N}{S_i / S} \quad (6)$$

260 where FR is the frequency ratio, N_i represents the account of landslides within the area
261 corresponding to the conditioning factor, N is the total number of landslides, S_i is the area
262 covered by the conditioning factor and S is the total area of the study region.

删除[肖巍峰]: where CF is the certainty factor for potential landslide occurrences, PP_a is the proportion of the number of landslide points relative to the area of the influencing factor's domain, and PP_s is the proportion of the total number of landslide points across the entire study region to the total area of the study region.

263 3.1.3 Buffer distance optimization and uncertainty assessment for LSP

264 To generate negative (non-landslide) samples for LSP, areas within buffer distances of d
265 $= 0.1, 0.5, 1.0, 2.0$, and 5.0 km around landslide locations were excluded, with balanced
266 negative samples ($n = 705$) randomly selected from remaining stable areas for each distance.
267 The optimal buffer distance was determined by evaluating SVM and LightGBM model
268 performance using AUC, Precision, Recall, and F1-score metrics.

269 The selection of buffer distances (0.1–5.0 km) was based on Zixing's geomorphological
270 considerations and practices commonly reported in LSP. This range encompasses multiple
271 spatial scales: slope-scale processes (0.1–0.5 km), catchment-scale features (1.0–2.0 km), and
272 regional-scale geological units (5.0 km). The evaluation ensures optimal spatial representation
273 without a priori assumptions about scale dependencies (Chang et al., 2023).

274 Prediction uncertainty was assessed using the mean and standard deviation (SD) of
275 predicted landslide susceptibility values. Lower mean and SD values indicate reduced
276 prediction uncertainty and more concentrated susceptibility patterns, suggesting higher model
277 confidence in LSP (Huang et al., 2022), thereby complementing the buffer distance
278 optimization process.

279 3.2 Effective rainfall threshold modeling

280 3.2.1 Rainfall parameterization and threshold calculation

281 Typhoon-induced landslides are generally influenced by a combination of antecedent
282 moisture conditions and immediate precipitation, rather than by isolated rainfall events
283 (Mondini et al., 2023; Tufano et al., 2021). To account for the cumulative impact of multi-day
284 rainfall while incorporating hydrological processes such as evapotranspiration and drainage,
285 we adopted the concept of effective rainfall (P_e), calculated as:

$$286 P_e = \sum_{i=0}^n k^i P_i \quad (7)$$

287 where P_i represents the daily rainfall on the i -th day preceding landslide occurrence, n denotes
288 the number of antecedent days considered, and k is the effective rainfall decay coefficient
289 (Segoni et al., 2018a). For hourly rainfall parameterization, P_i is derived as:

$$290 P_i = \sum_{j=1}^{24} R_{ij} \quad (8)$$

291 where R_{ij} is the hourly rainfall at the j -th hour of the i -th day.

292 3.2.2 Long-term and short-term rainfall parameters

删除[肖巍峰]: Negative (non-landslide) samples are generated by excluding zones within five buffer distances ($d=0.1, 0.5, 1.0, 2.0, 5.0$ km) around landslide points. For each distance d , negative samples are selected from the remaining stable areas, balanced to match the landslide count ($n=705$). The optimal buffer is determined by maximizing the receiver operating characteristic curve (AUC) values across distances.

3.1.4 Uncertainty assessment for model performance

To assess the SVM and LightGBM models' performance in predicting landslide susceptibility, we focused on the area under the AUC for both the training and test sets. AUC is a crucial metric for assessing classification models, especially in binary tasks like this. The AUC score quantifies the model's overall ability to distinguish between the positive (landslide) and negative (non-landslide) classes. An AUC value closer to 1 indicates better model performance, reflecting a higher capability to correctly classify instances.

In landslide susceptibility prediction, the mean and standard deviation (SD) are critical metrics indicating central tendency and variability. Generally, a lower mean and SD in LSP distribution suggest lower uncertainty and less spread in predicting landslide susceptibility (Huang et al., 2022).

设置格式[肖巍峰]: 字体: 加粗

293 Rainfall-triggered landslides are generally triggered by two dominant mechanisms:
294 prolonged low-intensity rainfall and short-duration high-intensity storms. Based on statistical
295 analysis of historical landslide events in Hunan Province (Xiao et al., 2025), a 7-day
296 antecedent period was identified as optimal for characterizing long-term rainfall impacts.
297 Consequently, the 7-day effective rainfall (D7) was selected as the long-term parameter.
298 Short-term rainfall metrics were defined as cumulative precipitation over 1 hour (H1), 12
299 hours (H12), 24 hours (H24), and 72 hours (H72) preceding landslide initiation. These
300 intervals capture distinct rainfall characteristics: H1 reflects extreme short-term intensity for
301 rapid slope failures, H12 and H24 represent sub-daily to daily precipitation critical for
302 intermediate responses, and H72 accounts for multi-day storm sequences.

303 **3.2.3 Rainfall threshold model development**

304 The threshold modeling framework comprises four sequential steps:

305 (1) Parameter calculation: For each landslide sample, short-term rainfall parameters (H1,
306 H12, H24, and H72) and the long-term rainfall parameter (D7) are calculated. The ratios of
307 short-term parameters to the long-term parameter are computed as: $R1=H1/D7$, $R12=H12/D7$,
308 $R24=H24/D7$, and $R72=H72/D7$.

309 (2) Threshold setting: Long-to-short-term ratio coefficients (RC1, RC12, RC24, and
310 RC72) are introduced as thresholds to determine the dominant rainfall pattern for each
311 landslide. These thresholds are used to classify landslides into short-term or long-term
312 Typhoon-induced categories.

313 (3) Coefficient optimization: A cyclic trial-and-error method is employed to determine
314 the optimal ratio coefficients (RC1, RC12, RC24, and RC72), maximizing the accuracy and
315 reliability of the model.

316 **3.2.4 Optimal ratio coefficient threshold determination**

317 The process of determining the optimal long-to-short-term ratio coefficient threshold is
318 demonstrated using H12-D7 as an example. The process for the remaining coefficients (H1-
319 D7, H24-D7, and H72-D7) follows a similar approach. A 5-fold cross-validation method is
320 applied, with the following procedure:

321 (1) Rainfall data extraction for landslide locations: For each of the 705 landslide points,
322 R12 and D7 values are extracted from these interpolated surfaces at the exact landslide
323 coordinates, ensuring that each landslide location receives rainfall values derived from the
324 spatially weighted contributions of all nearby gauge stations. R12 and D7 values for each
325 landslide are calculated using Equations (7) and (8).

326 (2) Data preparation: The dataset is divided into five equal parts for cross-validation,
327 with each part serving as a test set while the remaining four serve as the training set.

328 (3) Initial threshold setting: An initial threshold for RC12 is set based on the minimum
329 value in the training set.

330 (4) Threshold evaluation: For each fold, the RC12 threshold is compared with the R12
331 value of samples in the test set. If $RC12 < R12$, the prediction is considered a failure.
332 Prediction accuracy is calculated for each RC12 threshold, adjusting in 0.001 increments until
333 the highest prediction accuracy is achieved.

334 (5) Optimal RC12 threshold determination: The RC12 threshold with the highest
335 prediction accuracy is selected for each fold. The final RC12 threshold is determined by
336 averaging the optimal thresholds from all five folds.

337 3.2.5 Spatial distribution of optimal threshold

338 According to the optimal ratio coefficient threshold determined in section 3.2.4 and the
339 long-term and short-term rainfall parameters obtained through interpolation, the threshold
340 spatial distribution for the study area can be derived. Taking H12/D7 as an example, the
341 process is as follows:

删除[肖巍峰]: Spatial interpolation: Kriging interpolation is applied to short-term and long-term rainfall data from various rain gauge stations within the study area. R12 and D7 values for each landslide are calculated using Equations (7) and (8).

342 First, by dividing the H12 values of each landslide point by the optimal ratio coefficient
343 RC12, the corresponding D7 thresholds for each landslide point can be calculated. These D7
344 thresholds serve as a basis for applying the Kriging interpolation method to obtain the spatial
345 distribution map of the D7 thresholds across the entire study area.

346 Next, by multiplying the D7 values of each landslide point by the ratio coefficient RC12,
347 the corresponding H12 thresholds for each landslide point can be determined. Subsequently,
348 utilizing these H12 thresholds, the Kriging interpolation method is applied once more to
349 generate the spatial distribution map of the H12 thresholds for the entire study area.

350 **3.3 Typhoon-specific rainfall-induced landslide warning system**

351 | 删除[肖巍峰]: Typhoon-adapted hazard warning system

352 In order to effectively prevent typhoon-adapted landslide hazards, constructing a
353 comprehensive landslide early warning system is crucial. This system integrates landslide
354 susceptibility prediction with critical rainfall thresholds, combining spatial probability and
355 temporal probability to predict the risk of landslide occurrence and the timing of potential
356 events.

357 **3.3.1 Construction of the hazard warning system**

358 Using the natural breaks point method, the LSP is categorized into five levels of spatial
359 probability: very low (S1), low (S2), moderate (S3), high (S4), and very high (S5). These
360 levels represent varying degrees of susceptibility to landslides in different regions, forming
361 the basis for assessing landslide risks when combined with rainfall data. Paralleling the LSP
362 categorization, rainfall thresholds are also divided into five levels using the natural breaks
363 point method, representing temporal probability: very low (T1), low (T2), moderate (T3),
364 high (T4), and very high (T5). A lower rainfall threshold indicates a higher likelihood of
365 typhoon-induced landslides, thus signaling a greater risk of landslide events.

366 | **Table 2.** Classification of landslide hazard warning zones by integrating landslide susceptibility levels
367 (S1~S5) with rainfall threshold levels (T1~T5).

368 | 删除[肖巍峰]: 1

Landslide hazard warning zones	T1	T2	T3	T4	T5
-----------------------------------	----	----	----	----	----

S1 (very low)	No warning zone (2 nd level)	No warning zone (1 st level)			
S2 (low)	3 rd level warning zone	No warning zone (2 nd level)	No warning zone (2 nd level)	No warning zone (1 st level)	No warning zone (1 st level)
S3 (moderate)	4 th level warning zone	3 rd level warning zone	3 rd level warning zone	No warning zone (2 nd level)	No warning zone (1 st level)
S4 (high)	5 th level warning zone	4 th level warning zone	3 rd level warning zone	No warning zone (2 nd level)	No warning zone (1 st level)
S5 (very high)	5 th level warning zone	5 th level warning zone	4 th level warning zone	3 rd level warning zone	No warning zone (2 nd level)

367 The matrix-based integration of LSP results and rainfall thresholds, as presented in Table
 368 1 (Segoni et al., 2015), highlight the correlation between landslide susceptibility and rainfall
 369 intensity. As the levels of landslide hazard warnings escalate from the 1st level, indicating no
 370 warning, to the 5th level, which signifies the highest alert, the likelihood of landslide
 371 occurrences correspondingly increases. Areas categorized in higher hazard zones correspond
 372 to regions with a heightened risk of landslides. This hazard warning system provides a spatial
 373 framework for risk assessment and early warning, generating hazard zonation maps that can
 374 be integrated into operational landslide monitoring and warning protocols. This underscores
 375 the importance of implementing more effective geological disaster prevention strategies, as
 376 thoroughly discussed in the literature by Huang et al. (2022).

377 4. Landslide susceptibility prediction using machine learning models

378 4.1 Statistical analysis of conditioning factors

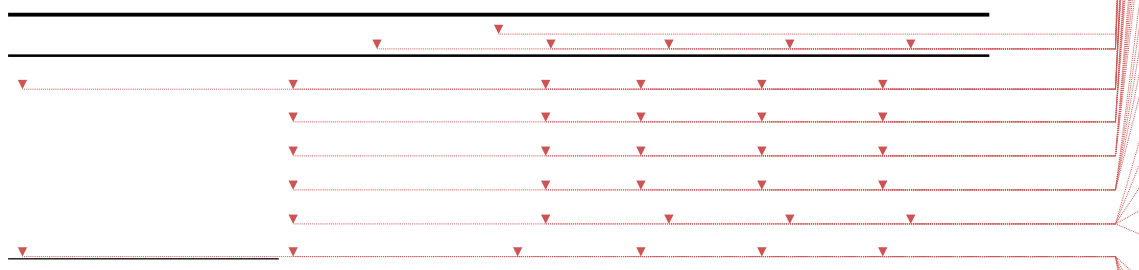
379 | 删除[肖巍峰]: IV, CF and FR values

379 The statistical analysis reveals distinct patterns of landslide susceptibility across all
 380 conditioning factors (Table S1 in the Supplement). Topographic factors demonstrate clear
 381 elevation-dependent behavior, with maximum susceptibility occurring at intermediate
 382 elevations (545-782 m, FR=1.637, IV=0.389), suggesting optimal conditions where
 383 weathering processes and slope instability converge. Slope gradient exhibits peak
 384 susceptibility in the moderate range (7.87-15.06°, FR=1.522, IV=0.343), indicating
 385 insufficient driving forces at gentler slopes and potential debris removal at steeper gradients.

386 South-facing aspects show enhanced susceptibility (FR=1.299, IV=0.230), likely attributable
387 to intensified weathering from solar radiation and moisture cycles.

388 Morphological indices reveal significant correlations with landslide occurrence. Profile
389 curvature demonstrates highest susceptibility in convex areas (0.17-0.59, FR=1.480,
390 IV=0.480), where stress concentration promotes slope failure. TWI shows strong positive
391 correlation with wetness, peaking at high values (8.69-13.62, FR=1.799, IV=0.444),
392 confirming the critical role of water accumulation in slope destabilization. SPI indicates
393 maximum susceptibility in moderate stream power ranges (1.27-2.39, FR=1.298, IV=0.229),
394 reflecting optimal erosional conditions.

395 Proximity factors exhibit contrasting patterns based on infrastructure type. Distance to
396 roads shows strong inverse correlation with landslide occurrence (0-800 m, FR=1.499,
397 IV=0.333), indicating anthropogenic disturbance effects. Conversely, distance to faults
398 reveals a bimodal pattern with peak susceptibility at intermediate distances (7-12 km,
399 FR=1.439, IV=0.305), suggesting regional structural influence rather than localized fault-
400 induced instability. Environmental factors demonstrate vegetation's protective role, with
401 moderate NDVI values (0.64-0.76) showing elevated susceptibility (FR=1.854, IV=0.015),
402 representing the transition zone between bare soil vulnerability and established vegetation
403 stability. Lithological analysis reveals pronounced material control, with rhyolite (FR=1.546,
404 IV=0.353) and granite (FR=1.247, IV=0.198) showing enhanced susceptibility due to
405 intensive weathering and joint development, while sedimentary rocks (slate, shale, limestone,
406 sandstone) exhibit strong resistance (FR<0.21) owing to their structural integrity and lower
407 weathering susceptibility.



删除[肖巍峰]: The IV, CF, and FR values were calculate...

删除[肖巍峰]: Factor grading

删除[肖巍峰]: Landslides

删除[肖巍峰]: IV

删除[肖巍峰]: CF

删除[肖巍峰]: FR

删除[肖巍峰]:

删除[肖巍峰]: 92~314

删除[肖巍峰]: 81

删除[肖巍峰]: -0.493

删除[肖巍峰]: -0.679

删除[肖巍峰]: 0.507

删除[肖巍峰]: 314~545

删除[肖巍峰]: 255

删除[肖巍峰]: 0.218

删除[肖巍峰]: 0.246

删除[肖巍峰]: 1.279

删除[肖巍峰]: 545~782

删除[肖巍峰]: 312

删除[肖巍峰]: 0.389

删除[肖巍峰]: 0.493

删除[肖巍峰]: 1.637

删除[肖巍峰]: 782~1098

删除[肖巍峰]: 57

删除[肖巍峰]: -0.505

删除[肖巍峰]: -0.704

删除[肖巍峰]: 0.495

删除[肖巍峰]: 1098~2033

删除[肖巍峰]: 0

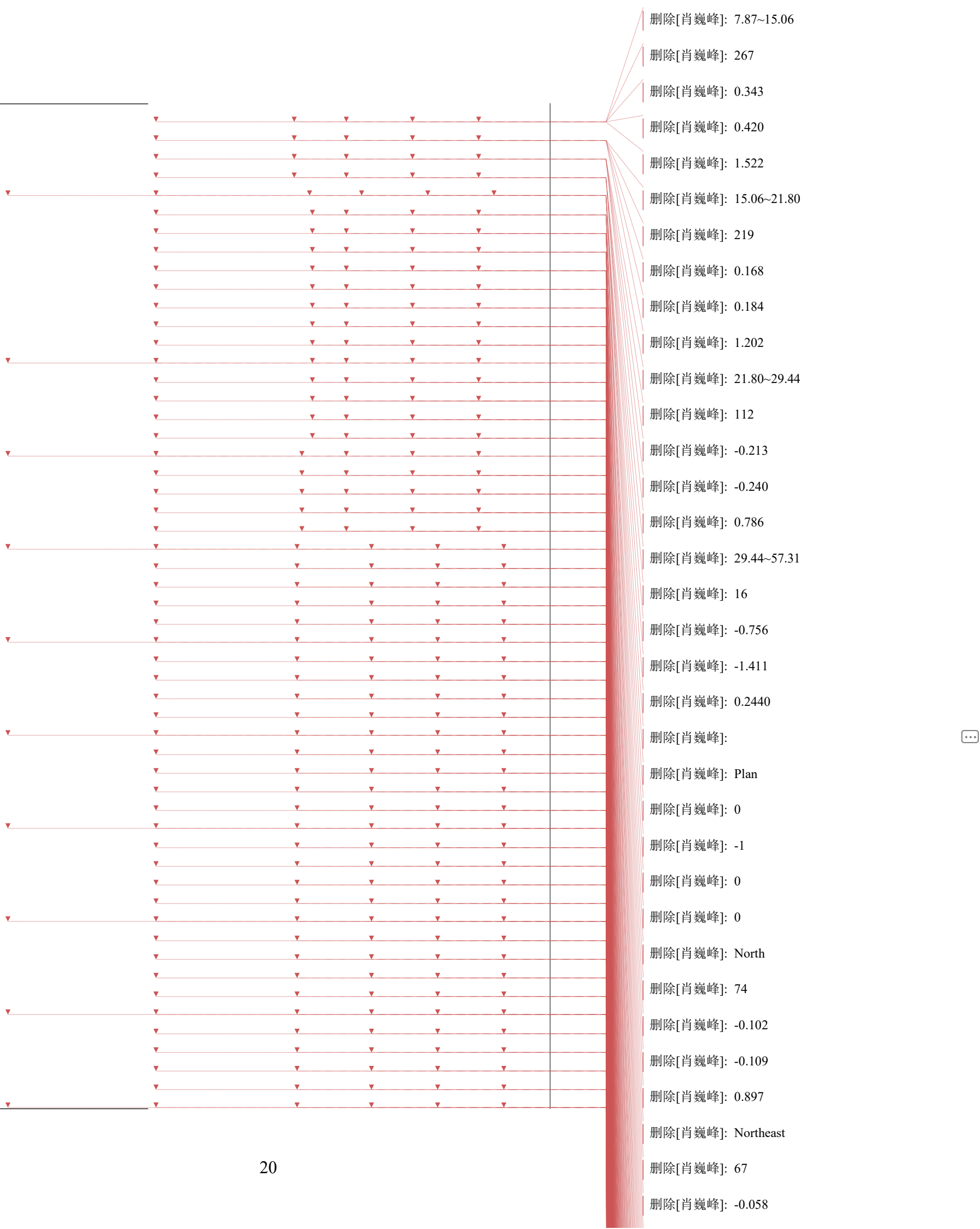
删除[肖巍峰]: -1

删除[肖巍峰]: 0

删除[肖巍峰]: 0

删除[肖巍峰]:

删除[肖巍峰]: 0~7.87



408

4.2 Landslide susceptibility modeling in Zixing City

409

Prior to model development, multicollinearity analysis was conducted using variance inflation factor (VIF) to ensure statistical reliability of the conditioning factors. The analysis revealed method-specific multicollinearity patterns: IV and CF methods showed no significant multicollinearity issues (all VIF < 10), while the FR method exhibited multicollinearity in four variables (SPI, Aspect, Plan curvature, and Distance to rivers with VIF > 10), which were subsequently excluded from FR-based modeling (Table S2 in the supplement). Following this preprocessing, landslide susceptibility prediction was performed using SVM and LightGBM models with the three distinct weighting methods (IV, CF, and FR). Susceptibility levels were categorized into five classes using the natural breaks classification method, with non-landslide samples strategically selected by excluding buffer zones of varying distances (0.1, 0.5, 1.0, 2.0, and 5.0 km) around documented landslide locations to optimize model performance and reduce spatial bias.

421

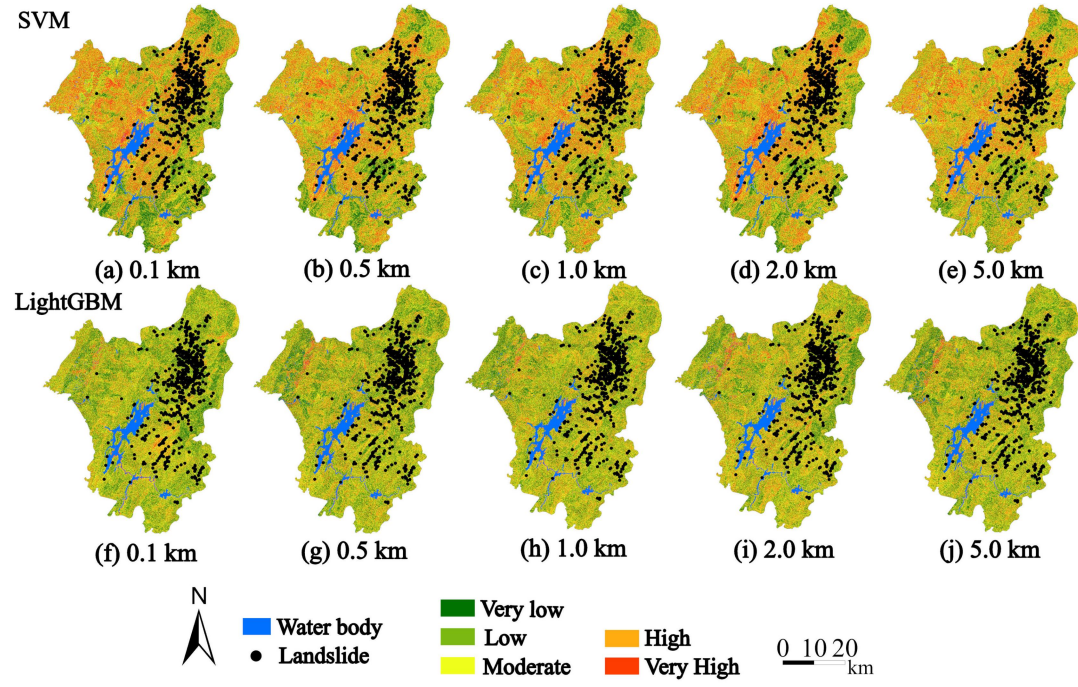
4.2.1 IV-based modeling performance

422

The IV-derived susceptibility maps (Fig. 4) revealed distinct spatial patterns between the two models across varying buffer distances. At smaller scales, the SVM model demonstrated more detailed classification, with a higher degree of overlap between high susceptibility areas and actual landslide locations. The LightGBM model's classification was smoother, with a lower degree of overlap between high susceptibility areas and actual landslide locations. Notably, this performance discrepancy diminished progressively with increasing buffer distances.

删除[肖巍峰]: Shale
 删除[肖巍峰]: 10
 删除[肖巍峰]: -0.798
 删除[肖巍峰]: -1.601
 删除[肖巍峰]: 0.202
 删除[肖巍峰]: Limestone
 删除[肖巍峰]: 1
 删除[肖巍峰]: -0.907
 删除[肖巍峰]: -2.376
 删除[肖巍峰]: 0.093
 删除[肖巍峰]: Sandstone
 删除[肖巍峰]: 3
 删除[肖巍峰]: -0.958
 删除[肖巍峰]: -3.179
 删除[肖巍峰]: 0.042
 删除[肖巍峰]: Granite
 删除[肖巍峰]: 485
 删除[肖巍峰]: 0.198
 删除[肖巍峰]: 0.221
 删除[肖巍峰]: 1.247
 删除[肖巍峰]: Rhyolite
 删除[肖巍峰]: 198
 删除[肖巍峰]: 0.353
 删除[肖巍峰]: 0.436
 删除[肖巍峰]: 1.546

设置格式[肖巍峰]: 段落间距段前: -21474800 行, 对齐
 删除[肖巍峰]: Multicollinearity analysis for landslide-
 删除[肖巍峰]: To ensure reliable landslide susceptibility
 删除[肖巍峰]: 3



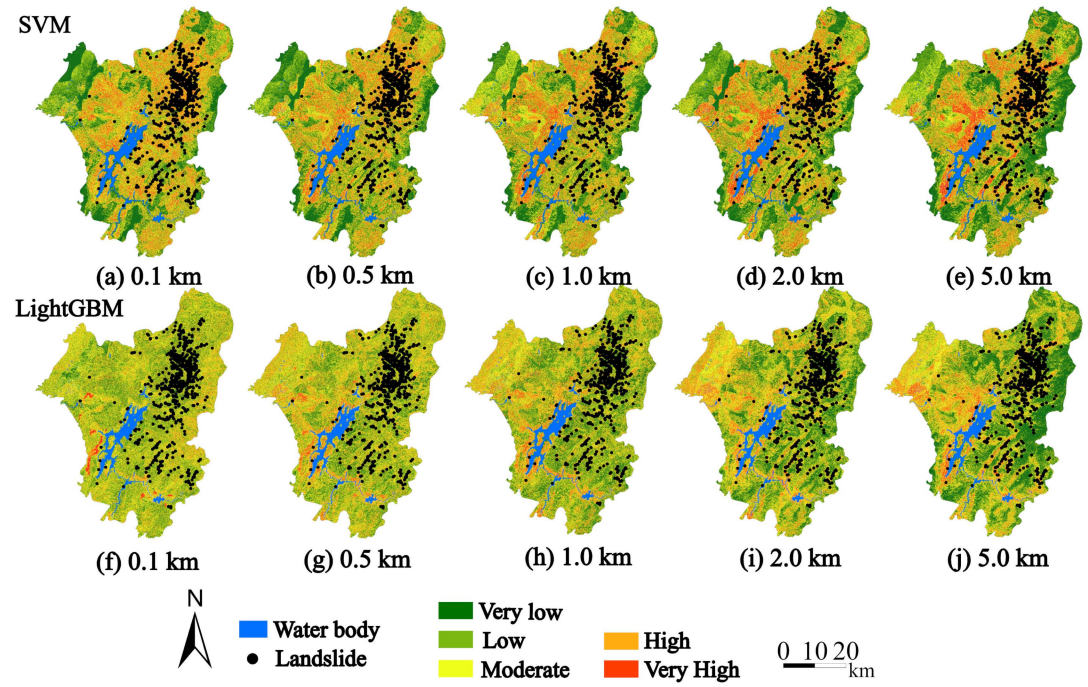
429

430

431 **Figure 4.** Landslide susceptibility map based on SVM and LightGBM models using the IV input.432 **4.2.2 CF-based modeling performance**

| 删 除 [肖巍峰]: 3

433 In CF-based modeling (Fig. 5), the SVM model's high and very high landslide
 434 susceptibility areas at smaller scales were more extensive than in the IV mode, with actual
 435 landslide locations more frequently distributed within these high-risk areas. As the scale
 436 increased, the high susceptibility areas gradually decreased. The LightGBM model also
 437 showed a relatively smooth distribution, with some high susceptibility areas identified at
 438 smaller scales gradually integrating as the scale increased, following a similar trend to the
 439 SVM model.

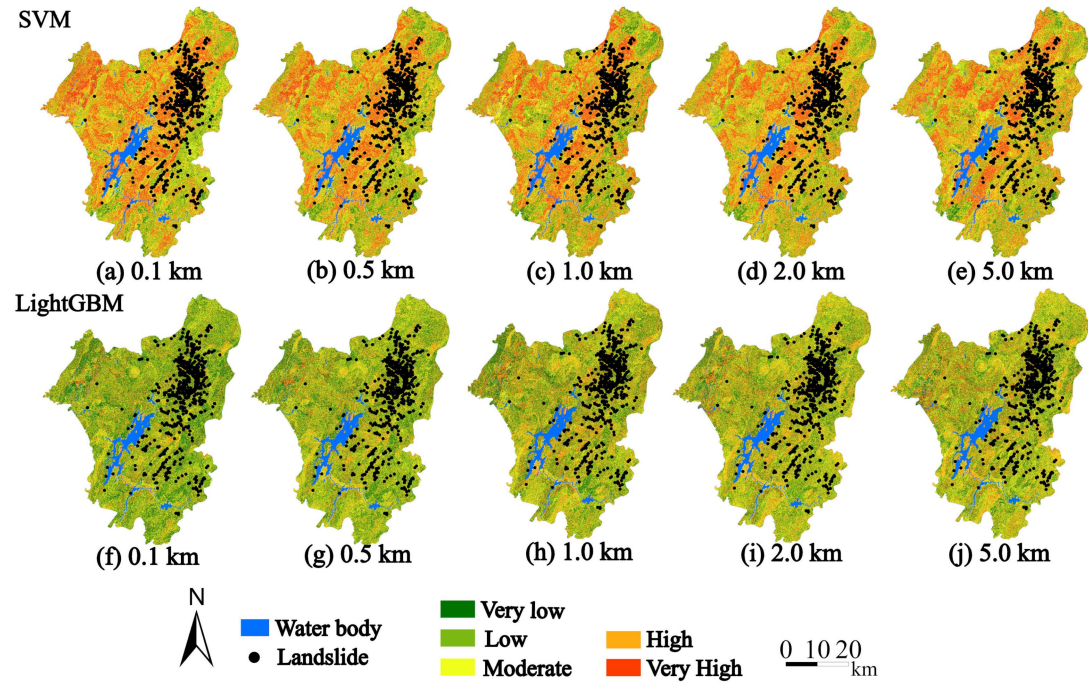


440
441 **Figure 5.** Landslide susceptibility map based on SVM and LightGBM models using the CF input.

442 **4.2.3 FR-based modeling performance**

443 删除[肖巍峰]: 3

444 Regarding the FR input (Fig. 6), the SVM model identified a significant number of high
 445 and very high landslide susceptibility areas at smaller scales compared to the IV and CF
 446 inputs, which closely matched the actual locations of landslides. As the buffer scale expanded,
 447 these high-risk areas generally diminished and the distribution became smoother. Conversely,
 448 the LightGBM model delivered more uniform results, offering broader moderate-risk
 449 distributions, with a small number of high susceptibility areas that did not align with the
 450 actual landslide locations. As the scale increased, the high susceptibility areas identified by
 451 the LightGBM model gradually diminished, showing greater consistency with the SVM
 452 model results at the higher scale.



454
455 **Figure 6.** Landslide susceptibility map based on SVM and LightGBM models using the FR input.

456 **4.3 Uncertainty analysis of LSP results**

457 **4.3.1 LSP accuracy evaluation and comparative performance**

458
459 Table S2 (in the Supplement) demonstrates contrasting performance characteristics
460 between the two machine learning approaches across different spatial scales and input
461 configurations. LightGBM consistently achieved high AUC values (0.915-0.921) and
462 maintained stable F1-scores (0.838-0.850) across all buffer distances and input methods,
463 indicating robust generalization capability. In contrast, SVM exhibited pronounced sensitivity
464 to parameter combinations, with performance varying significantly across different buffer
465 distances (F1-scores ranging from 0.681 to 0.859) and input methods, particularly showing
466 notable degradation with FR input at extreme spatial scales (0.1 km and 5.0 km).

467 Two configurations emerged as comprehensively superior: SVM with FR input at 0.5 km
468 and 2.0 km buffer distances, both achieving F1-scores of 0.859. These optimal configurations
469 not only maintained competitive AUC values (0.914 and 0.913 respectively) but demonstrated

刪除[肖巍峰]: 4

刪除[肖巍峰]: 4

刪除[肖巍峰]: Table 3 presents the training and testing AUC values of SVM and LightGBM models across buffer distances (0.1–5.0 km) and input methods (IV, CF, FR). Both models demonstrated robust predictive performance, with LightGBM consistently outperforming SVM, particularly under FR in ...

470 superior precision-recall balance compared to corresponding LightGBM configurations (F1-
471 scores: 0.854 and 0.856). The high recall values (0.845 and 0.851) coupled with robust
472 precision (0.873 and 0.867) indicate enhanced sensitivity to landslide-prone areas while
473 minimizing false positive predictions. This bimodal performance pattern suggests that
474 intermediate buffer distances effectively capture fault-related geomorphological processes
475 influencing slope stability.

476 Independent validation on the test set confirmed the robustness of these optimal
477 configurations, with SVM-FR models at 0.5 km and 2.0 km buffer distances achieving F1-
478 scores of 0.847 and 0.852 respectively, representing minimal performance degradation from
479 training results. The consistent AUC values (0.909 and 0.908) on the test set further validate
480 the models' discriminative capability and indicate absence of overfitting, confirming the
481 reliability of these configurations for practical landslide susceptibility assessment applications.

482 4.3.2 LSP distribution characteristics across conditions

483 | 删除[肖巍峰]: 4

483 In addition to the performance metrics, the distribution characteristics of landslide
484 susceptibility predictions revealed fundamental differences between the models (Figs. S1–S3
485 in the Supplement). LightGBM generated smoother, more symmetrical distributions with
486 lower mean susceptibility values (0.196–0.320) and smaller standard deviations (0.099–
487 0.187), indicating stable and uniform predictions. In contrast, SVM exhibited greater
488 variability, with irregular distributions, higher mean values (0.303–0.515), and larger standard
489 deviations (0.112–0.214). Notably, SVM's mean susceptibility under FR input rose sharply
490 (0.446–0.515), while LightGBM maintained lower means despite moderately broader
491 deviations (0.160–0.187).

492 | 删除[肖巍峰]: Supplement Figs. S1–S3

492 Therefore, SVM is preferable for FR-based modeling at 0.5 km and 2.0 km buffers,
493 where spatial precision is prioritized over prediction uniformity. The SVM model achieved its
494 highest accuracy at the 0.5 km buffer, classifying 86.4% of recorded landslides in high and

495 very high susceptibility zones (Fig. 6 (b)). At the 2.0 km buffer (Fig. 6 (d)), it still correctly
496 classified 82.1% of landslides in these zones. As a result, Fig. 6 (b) is selected as the final
497 landslide susceptibility map.

498 5 Landslide risk assessment in Zixing City

499 5.1 Critical rainfall thresholds for landslides in Zixing City

500 four rainfall threshold models (H1-D7, H12-D7, H24-D7, and H72-D7) through 5-fold
501 cross-validation, with their optimal ratio coefficient (RC) thresholds and prediction accuracies
502 summarized in Table 3. The H24-D7 model, coupling 24-hour rainfall during landfall with 7-
503 day antecedent moisture, achieved the highest accuracy (71.8%) by effectively capturing both
504 cumulative saturation and abrupt triggering by typhoon rainfall bursts. Notably, the H24-D7
505 model exhibited stable performance across all folds, with accuracy ranging narrowly between
506 68.8% (Fold 1) and 74.6% (Fold 4), reflecting robust generalizability.

507 **Table 3.** Optimal RC values and prediction accuracies (%) for each model across 5-fold cross validation.

Model	Fold 1 RC/Accuracy	Fold 2 RC/Accuracy	Fold 3 RC/Accuracy	Fold 4 RC/Accuracy	Fold 5 RC/Accuracy	Average RC/Accuracy
H1-D7	0.032/56.5	0.062/29.7	0.076/35.5	0.022/53.6	0.040/47.8	0.047/44.6
H12-D7	0.077/54.2	0.167/46.6	0.243/48.3	0.267/47.7	0.154/45.3	0.182/48.5
H24-D7	0.472/68.8	0.436/72.3	0.422/73.1	0.459/74.6	0.414/70.2	0.440/71.8
H72-D7	0.789/56.5	0.776/59.4	0.781/63.1	0.802/51.4	0.783/60.1	0.787/58.1

508 In contrast, the H1-D7 and H12-D7 models displayed marked instability: H1-D7
509 accuracy fluctuated between 29.7% (Fold 2) and 56.5% (Fold 1), while H12-D7 thresholds
510 (RC12: 0.077–0.267) corresponded to accuracies of 45.3–48.3%. The H72-D7 model showed
511 moderate performance variability (accuracy: 51.4–63.1%) despite consistently high RC72
512 thresholds (>0.78).

513 These results highlight the critical role of temporal rainfall parameter selection. The
514 superior performance of the H24-D7 model (24-hour short-term rainfall and 7-day antecedent
515 rainfall) suggests that a 24-hour duration optimally captures both immediate landslide triggers

删除[肖巍峰]: The July 2024 typhoon Gaemi-induced extreme rainfall (412.7 mm average, peaking at 673.9 mm/24h and 132.2 mm/h) triggered a heavy landslide event in Zixing City, Hunan. This event, characterized by granite-weathered soils and slope-side settlements, highlighted critical thresholds for typhoon-induced failures.

删除[肖巍峰]: Four rainfall threshold models (H1-D7, H12-D7, H24-D7, and H72-D7) were systematically evaluated through 5-fold cross-validation

删除[肖巍峰]: 4

删除[肖巍峰]: The H24-D7 model, which couples 24-hour landfall rainfall with 7-day antecedent moisture—key components of typhoon hydrology—achieved the highest accuracy (71.8%), effectively capturing both cumulative saturation and abrupt triggering by typhoon rainfall bursts

删除[肖巍峰]: 4

516 and cumulative hydrological effects, balancing sensitivity and stability. Shorter (H1/H12) or
 517 longer (H72) durations either overemphasize transient rainfall spikes or dilute critical
 518 triggering signals.

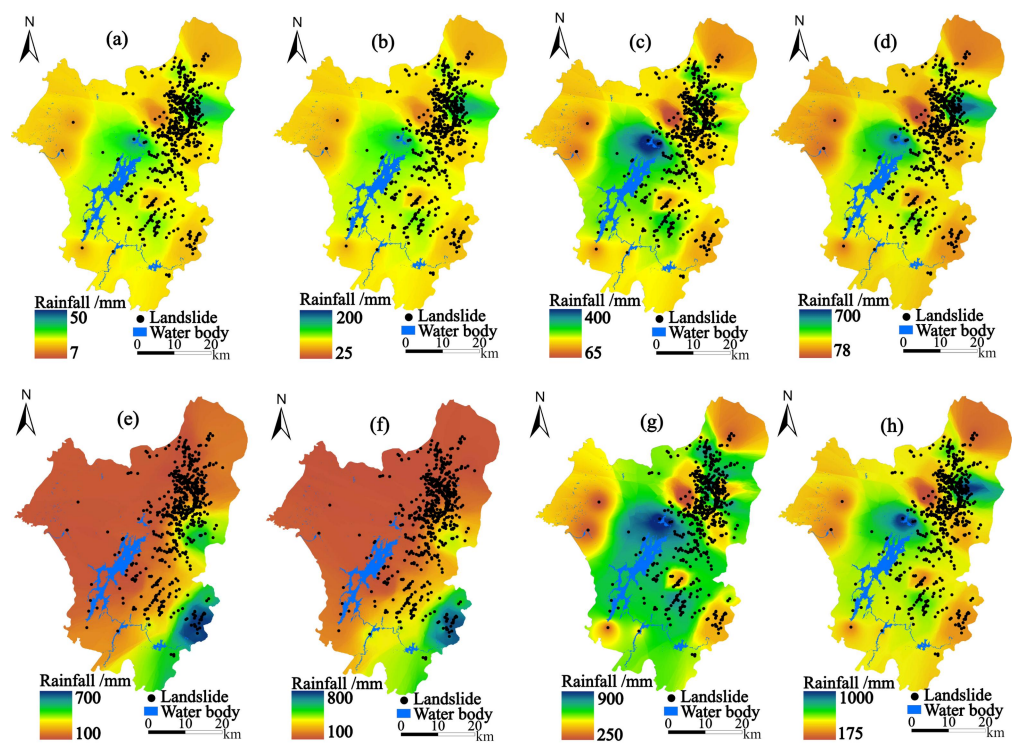
519 5.2 Spatio-temporal distribution of rainfall thresholds

520 Fig. 7 illustrates the spatial distribution of rainfall-triggered landslide thresholds derived
 521 from four models (RC1, RC12, RC24, and RC72) across multiple temporal scales (1-hour,
 522 12-hour, 24-hour, 72-hour, and 7-day) within the study area.

523 5.2.1 Short-term predictions (1-hour to 12-hour scales)

524 At the 1-hour scale (Fig. 7 (a)), the RC1 model generated thresholds ranging from 7 to
 525 50 mm, with 65.2% of landslides occurring in moderate threshold zones (20-30 mm). This
 526 indicates the model's effectiveness in detecting slope failures under short-duration rainfall. In
 527 contrast, the RC12 model on the 12-hour scale (Fig. 7 (b)) showed a wider threshold range
 528 (25-200 mm), with 62.9% of landslides in mid-to-high threshold regions (80-130 mm). This
 529 mismatch suggests that the 12-hour cumulative data may underestimate rainfall impacts in
 530 specific topographic settings.

删除[肖巍峰]: The superior performance of the H24-D7 model—combining 24-hour short-term rainfall (H24) and 7-day antecedent rainfall (D7)—suggests that a 24-hour duration optimally captures both immediate landslide triggers and cumulative hydrological effects, balancing sensitivity and stability. This contrasts with shorter (H1/H12) or longer (H72) durations, which either overemphasize transient rainfall spikes or dilute critical triggering signals



532 [Figure 7 Distribution of typhoon rainfall thresholds under various optimal RC ratios: \(a\) 1-hour RC1-based,](#)
533 [\(b\) 12-hour RC12-based, \(c\) 24-hour RC24-based, \(d\) 72-hour RC72-based, \(e\) 7-day RC1-based, \(f\) 7-day](#)
534 [RC12-based, \(g\) 7-day RC24-based, and \(h\) 7-day RC72-based.](#)

535

536 **5.2.2 Mid-term predictions (24-hour to 72-hour scales)**

537 The RC24 model at the 24-hour scale (Fig. 7 (c)) displayed a threshold range of 65-400
538 mm, with 87.1% of landslides occurring within moderate thresholds (100-250 mm) and
539 12.3% in higher thresholds (>250 mm). This indicates a more accurate capture of rainfall
540 intensity effects. At the 72-hour scale (Fig. 7 (d)), the RC72 model produced thresholds
541 between 78-700 mm, with 59.2% of landslides in mid-to-high threshold regions (200-500
542 mm). Although the RC72 model demonstrated reasonable sensitivity to prolonged rainfall, its
543 upper threshold (700 mm) may result in conservative risk predictions for some geological
544 settings.

545 **5.2.3 Long-term predictions (7-day scale)**

546 At the 7-day scale, significant differences emerge across models in terms of predicted
547 rainfall thresholds and landslide points. The RC1 model (Fig. 7 (e)) shows a threshold range
548 of 100-700 mm, with landslide points predominantly concentrated in the lower rainfall ranges.
549 While these low-threshold landslides may indicate localized risks, the model's conservative
550 threshold distribution fails to effectively capture landslides triggered by higher rainfall
551 amounts, potentially overlooking more significant events.

552 The RC12 model (Fig. 7 (f)), with a threshold range of 100-800 mm, also shows a
553 concentration of landslide points in the lower rainfall ranges. Despite a wider threshold range,
554 the similarity to the RC1 model suggests that RC12 may also underutilize its capacity to
555 predict higher typhoon-induced landslides, leading to under-prediction in areas experiencing
556 moderate to heavy precipitation.

557 In contrast, the RC24 model (Fig. 7 (g)) exhibits a balanced threshold range (250-900
558 mm) and effectively identifies landslide points in both moderate and high rainfall categories.

删除[肖巍峰]: **Figure 7.** Distribution of typhoon rainfall thresholds under the optimal RC ratio in Zixing City.

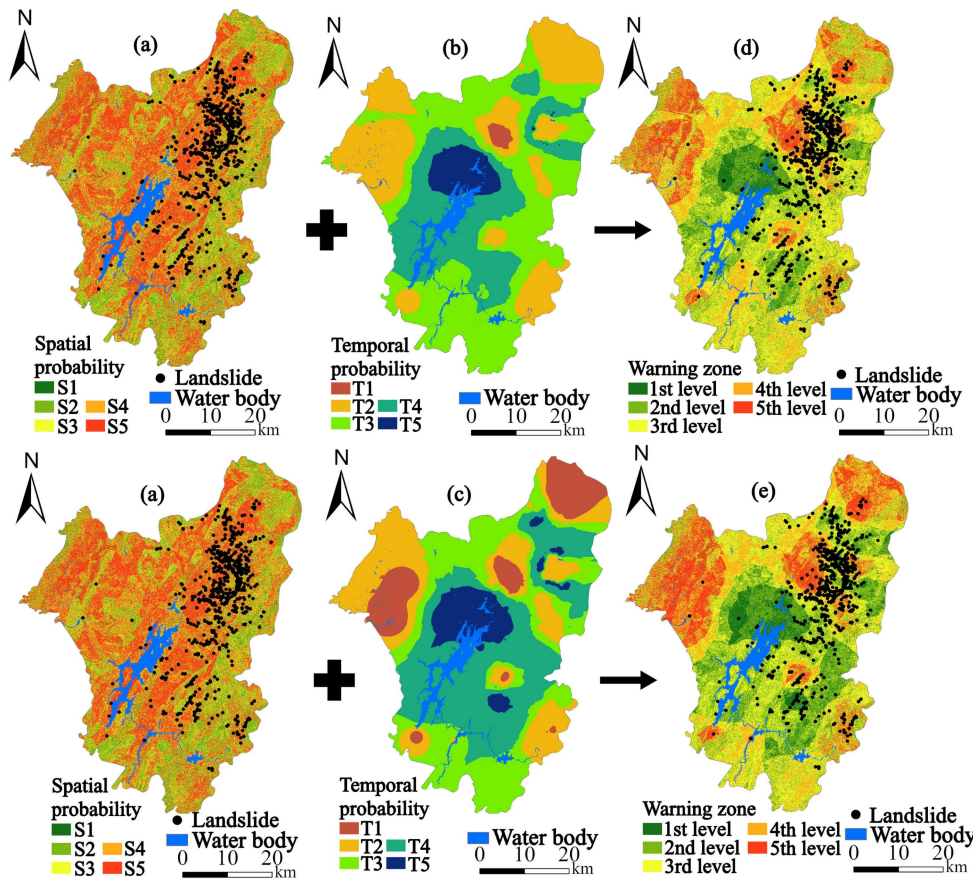
559 This balance enables RC24 to capture the full spectrum of typhoon-induced landslides,
560 accurately identifying risks across different rainfall intensities.

561 The RC72 model (Fig. 7 (h)) shows a concentration of landslide points in the higher
562 rainfall range (175-1000 mm). While it predicts landslides accurately under heavy rainfall
563 conditions, the model may overestimate risks in some regions and neglect potential landslides
564 associated with lower rainfall thresholds.

565 Based on the above analysis, the RC24 model is the optimal choice, which aligns with
566 the finding in Section 5.1. Its effectiveness is evident as it demonstrates superior stability and
567 accuracy in both the 24-hour and 7-day timescales. The RC24 model's balanced threshold
568 range enables it to effectively capture landslide risks across varying rainfall intensities,
569 making it the most reliable choice for practical applications in landslide disaster early warning
570 systems.

571 **5.3 Landslide hazard warning system for Zixing City**

572 Based on the optimal LSP results (Fig. 6 (b)) and the validated RC24 rainfall threshold
573 model, a spatially explicit landslide hazard warning system was established for Zixing City.
574 The integration of spatial probability (LSP) and temporal probability (rainfall thresholds)
575 followed the matrix classification outlined in Table 1.



576

577 **Figure 8** Landslide warning zones generated by overlaying spatial and temporal probability maps: (a) optimal
 578 spatial probability, (b) 24-hour RC24-based rainfall threshold, (c) 7-day RC24-based rainfall threshold, (d)
 579 overlay of (a) and (b), and (e) overlay of (a) and (c).

580 Five susceptibility levels in the LSP map (Fig. 6 (b)) were replaced with five spatial

581 probabilities (S1–S5) (Fig. 8 (a)), respectively. Simultaneously, the spatially interpolated 24-
 582 hour rainfall thresholds (H24) (Fig. 8 (b)) and 7-day effective rainfall thresholds (D7) (Fig. 8
 583 (c)) derived from the RC24 model were classified into five temporal probability levels (T1–
 584 T5) using the natural breaks method. Spatial overlay analysis was performed to combine the
 585 susceptibility levels (S1–S5) with the rainfall threshold levels (T1–T5), generating two hazard
 586 warning zone maps: [H24-based \(Fig. 8 \(d\)\) and D7-based \(Fig. 8 \(e\)\)](#).

587 Quantitative assessment of both warning systems reveals distinct performance
 588 characteristics. The 24-hour threshold system (Fig. 8 (d)) demonstrates superior predictive
 589 efficiency, with 71.4% of historical landslides occurring within high to very high warning
 590 zones (Levels 3–5) while covering only 34.2% of the total area, resulting in an efficiency ratio
 591 of 2.09 and a risk density of 49.0 landslides per 1000 high-risk grid cells. The spatial

删除[肖巍峰]: **Figure 8.** Landslide hazard warning zones in Zixing City.

删除[肖巍峰]: one based on the 24-hour rainfall thresholds (H24-D7) (Fig. 8 (d)) and the other on the 7-day effective rainfall thresholds (D7-H24) (Fig. 8 (e))

592 distribution shows concentrated high-risk areas primarily in the central region, characterized
593 by steep slopes ($>21.80^\circ$), weathered granite lithology, and road proximity (0–800 m). This
594 focused distribution indicates effective identification of areas most sensitive to short-term
595 intense rainfall triggers.

596 The 7-day threshold system (Fig. 8 (e)) exhibits broader spatial coverage, with high-risk
597 zones encompassing 42.7% of the study area and capturing 68.7% of historical landslides,
598 yielding a lower efficiency ratio of 1.61 and risk density of 37.8 landslides per 1000 grid cells.
599 This system effectively identifies extended vulnerable areas in northern and eastern regions,
600 reflecting cumulative rainfall effects on slope stability. The expanded coverage captures zones
601 where prolonged antecedent moisture interacts with moderate-to-high susceptibility
602 conditions.

603 Statistical validation confirms the complementary nature of both systems. The 24-hour
604 system achieves higher spatial efficiency (efficiency ratio 2.09 vs. 1.61) and landslide
605 concentration (risk density 49.0 vs. 37.8), making it optimal for immediate typhoon response
606 and targeted emergency resource allocation. Conversely, the 7-day system provides
607 comprehensive coverage for prolonged rainfall scenarios, essential for early warning during
608 extended typhoon events despite its broader spatial distribution and lower concentration
609 efficiency. The combined application of both systems enables dynamic hazard assessment,
610 addressing both rapid-onset failures during typhoon landfall and delayed failures following
611 sustained precipitation.

612
613 **6 Discussion**

614 **6.1 Optimization of landslide susceptibility prediction**

615 Our comparative analysis of SVM and LightGBM models across different input methods
616 (IV, CF, FR) and buffer distances revealed important insights into the optimization of LSP

删除[肖巍峰]: In the 24-hour threshold system (Fig. 8 (d)), a significant portion of the study area was classified as high to very high warning zones (Levels 3–5), particularly in the central region. These areas are characterized by steep slopes ($>21.80^\circ$; yellow to dark red regions in Fig. 2 (b)), weathered granite lithology (pink areas in Fig. 2 (l)), proximity to roads (0–800 m; blue zones in Fig. 2 (g)), and moderate-to-distant distances from fracture zones (2,000–7,000 m; light green regions in Fig. 2 (i)). The high-susceptibility zones (S4–S5), combined with lower rainfall thresholds (T4–T5), indicate acute sensitivity to short-term intense rainfall. Notably, these high-level warning zones overlap with 71.4% of historical landslide occurrences, underscoring the immediate threat posed by short-duration heavy rainfall events.

In contrast, the 7-day threshold system (Fig. 8 (e)) exhibits a similar distribution of high to very high warning zones (Levels 3–5) but with expanded coverage into the northern and eastern parts of the study area. These regions reflect the interaction of prolonged antecedent rainfall (D7) with moderate-to-very-high susceptibility (S3–S5). Topographically, these areas feature greater rainfall accumulation (steep slopes in Fig. 2 (b)) and are predominantly underlain by granite lithology (large pink zones in Fig. 2 (l)). Additionally, they are adjacent to roads (blue and green regions in Fig. 2 (g)) and closer to fracture zones (green and light yellow areas in Fig. 2 (i)). This broader spatial distribution captures sustained risks associated with cumulative rainfall, highlighting zones vulnerable to prolonged precipitation. The alignment of these warning zones with 68.7% of historical landslide sites further validates the effectiveness of the 7-day model in detecting cumulative hydrological effects.

617 under typhoon-specific rainfall conditions. SVM's superior performance at buffer distances of
618 0.5–2.0 km with FR inputs highlights the importance of spatial scale selection in typhoon-
619 induced landslide modeling. This extends existing research (Kalantar et al., 2018; Bogaard
620 and Greco, 2018) by identifying typhoon-specific spatial patterns that diverge from
621 conventional rainfall scenarios.

622 The optimal 0.5–2.0 km buffer range corresponds to the spatial autocorrelation pattern of
623 typhoon-induced failures, where intense moisture infiltration generates discrete instability
624 zones. This differs markedly from earthquake-triggered landslides, which cluster at finer
625 scales (Fan et al., 2019), reflecting typhoons' distinct hydrological impact. The effectiveness
626 of FR weighting is consistent with the findings of Reichenbach et al. (2018) and Yan et al.
627 (2019), who demonstrated that frequency-based methods effectively capture non-linear
628 relationships between factors in complex terrain. Our findings indicate FR's particular
629 strength under typhoon conditions stems from its capacity to capture specific factor
630 interactions, including how road networks intensify runoff concentration on weathered granite
631 slopes (Liu et al., 2022).

632 **6.2 Rainfall threshold modeling and typhoon-specific mechanisms**

633 The H24-D7 model's superior performance (71.8% accuracy) marks a significant
634 advancement in understanding the triggering mechanisms of typhoon-specific landslides. This
635 temporal window effectively captures the dual-phase nature of typhoon-induced slope failure:
636 prolonged antecedent saturation from tropical moisture bands followed by critical threshold
637 exceedance during typhoon core passage (Kirschbaum and Stanley, 2018). The model's
638 effectiveness validates the conceptual framework proposed by Nolasco-Javier and Kumar
639 (2018), who emphasized the importance of multi-temporal rainfall accumulation in tropical
640 cyclone environments.

删除[肖巍峰]: The comparative analysis of SVM and LightGBM models across different input methods (IV, CF, FR) and buffer distances revealed important insights into the optimization of landslide susceptibility prediction under typhoon rainfall conditions. While LightGBM generally exhibited higher overall accuracy and stability, SVM demonstrated superior performance at specific spatial scales (0.5–2.0 km buffers), capturing localized slope instability patterns induced by typhoon-driven hydrological processes. This finding aligns with previous studies highlighting SVM's effectiveness in modeling non-linear interactions between typhoon rainfall intensity and terrain features (Kalantar, 2018; Zhao et al., 2021).

The optimal performance of SVM at intermediate buffer distances (0.5–2.0 km) suggests a critical balance between typhoon-induced local heterogeneity (e.g., soil saturation variations) and regional geological controls. This range effectively isolates slope units most vulnerable to short-duration typhoon rainfall pulses, while filtering out noise from distant stable areas. The superiority of the FR input method underscores its ability to quantify typhoon-specific factor interactions, such as road density amplifying runoff concentration in granite-weathered slopes (Liu et al., 2022). These results emphasize the necessity of typhoon-adapted spatial scaling in susceptibility modeling, supporting the spatial correlation principles established by Reichenbach et al. (2018).

删除[肖巍峰]: **spatio-temporal distribution**

641 The spatial heterogeneity in rainfall thresholds reflects the complex interaction between
642 typhoon structure and local topography (Lee et al., 2018; Cho et al., 2022). Higher thresholds
643 in southeastern slopes (>250 mm) correspond to areas of enhanced orographic lifting (Fig.
644 7(c)), where terrain amplifies typhoon rainfall through forced ascent mechanisms. Conversely,
645 lower thresholds in northern valleys (100-150 mm) (Fig. 7(c)) indicate areas where
646 topographic channeling and moisture convergence create favorable conditions for slope
647 failure at reduced precipitation levels. This spatial variability contradicts the assumption of
648 uniform regional thresholds commonly applied in operational warning systems (Segoni et al.,
649 2018b) and supports the implementation of spatially distributed threshold approaches.

650 The H24-D7 model's robust cross-validation performance (68.8-74.6% across folds)
651 demonstrates its stability across different typhoon sub-events and rainfall patterns. This
652 consistency is crucial for operational implementation, as typhoons exhibit significant internal
653 variability in rainfall distribution and intensity (Liu et al., 2017). The model's ability to
654 maintain predictive accuracy across this variability represents a substantial improvement over
655 traditional empirical threshold approaches that often fail during extreme events (Guzzetti et al.,
656 2020).

657 6.3 Integration of susceptibility and rainfall thresholds for **landslide** warning

658 Integrating landslide susceptibility and rainfall thresholds in an early warning system
659 creates a dynamic framework for real-time monitoring and assessment of landslide hazards.
660 By overlaying static susceptibility maps with real-time precipitation data, this approach offers
661 a continuous hazard assessment that adapts to changing weather conditions, particularly
662 during typhoons. The system updates hazard assessments hourly, reflecting the evolving
663 precipitation patterns that drive landslide potential.

664 The operational framework consists of three hierarchical components: (1) static
665 susceptibility surfaces derived from optimized Support Vector Machine-based Flood Risk

删除[肖巍峰]: The evaluation of multiple rainfall threshold models (H1-D7, H12-D7, H24-D7, and H72-D7) revealed that the H24-D7 model was the most effective for predicting typhoon-triggered landslides. This model combines 24-hour typhoon rainfall bursts with 7-day antecedent moisture from tropical cyclones, achieving an accuracy of 71.8%. It strikes a balance between capturing immediate slope failure during typhoon landfall and accounting for prolonged saturation due to pre-typhoon rainfall. In contrast, the shorter (H1/H12) and longer (H72) durations misrepresented the rainfall dynamics specific to typhoons. This finding aligns with Long et al. (2020), who emphasized the importance of integrating both short-term intensity and long-term saturation to predict debris flows.

Spatial thresholds derived from the H24-D7 model demonstrated distinct rainfall gradients related to typhoon exposure. In southeastern slopes, which are more exposed to prevailing typhoon tracks (Fig. 7c), higher thresholds (>250 mm) were observed. This is consistent with Cai et al. (2023), who found that areas directly in the path of typhoons typically experience more intense rainfall due to the influence of the typhoon's core. These regions are often impacted by the high-intensity convective cores of typhoons. In contrast, northern valleys, influenced by cumulative typhoon rainbands, exhibited lower thresholds (100-150 mm). As Lin et al. (2019) pointed out, typhoon rainbands generate widespread, cumulative rainfall that can be further amplified by topography, such as in valleys where terrain traps moisture and enhances precipitation accumulation. This mechanism explains the lower triggering thresholds in these regions compared to the slopes directly exposed to typhoon tracks.

The spatial gradient observed in the H24-D7 thresholds reflects the dual rainfall modes of typhoons: convective cores with high-intensity bursts and stratiform bands with prolonged drizzle. This highlights the need for typhoon-specific models that can capture both microscale (e.g., storm cell) and macroscale (e.g., rainband) dynamics. Many existing models fail to address these complexities (Segoni et al., 2018b; Guzzetti et al., 2020). The H24-D7 model, by incorporating these spatial gradients and rainfall modes, represents a significant advancement in accurately predicting typhoon-induced landslides.

删除[肖巍峰]: hazard

666 (SVM-FR) models, which act as baseline hazard zones, (2) dynamic threshold surfaces (H24
667 and D7) that define conditions under which rainfall triggers landslide activation, and (3) real-
668 time precipitation monitoring, which drives continuous hazard updates. These components
669 work together to ensure a comprehensive and up-to-date hazard assessment.

670 One of the key features of this system is its ability to automatically adjust warning levels
671 based on meteorological forecasts. When forecasts indicate a greater than 70% probability of
672 threshold exceedance in high-susceptibility areas, the system escalates warning levels
673 accordingly, providing timely alerts to mitigate disaster risk (Piciullo et al., 2018). The dual-
674 threshold configuration enhances this approach by providing temporal staging suited to the
675 dynamic nature of typhoons. Specifically, as a typhoon approaches (48-72 hours before
676 landfall), the D7 threshold monitors antecedent rainfall to identify areas nearing saturation
677 and instability. As the typhoon intensifies and makes landfall, the H24 threshold responds to
678 immediate, intensive rainfall events, triggering warnings for zones that experience rapid
679 threshold exceedance (Gariano et al., 2015). This staged warning system ensures optimized
680 lead times for alerts, while also minimizing the risk of alert fatigue, a common challenge in
681 continuous hazard monitoring (Nocentini et al., 2024).

682 Unlike traditional point-based threshold systems, which are limited in their ability to
683 account for spatial variability across complex terrain, this approach integrates spatially
684 continuous thresholds. This design allows the system to address terrain-induced variability in
685 rainfall-triggered landslides while maintaining computational efficiency for regional-scale
686 applications (Calvello and Piciullo, 2016; Sun et al., 2024). Moreover, by incorporating
687 typhoon-specific rainfall parameterization within probabilistic threshold surfaces, this system
688 significantly advances beyond existing point-based hazard mapping approaches (Guzzetti et
689 al., 2020; Nolasco-Javier and Kumar, 2018).

690 For effective operational deployment, the system must be integrated with meteorological
691 monitoring infrastructure, such as weather radar networks and automated rainfall stations.
692 Critical components of implementation include real-time data processing capabilities,
693 standardized protocols for disseminating warnings, and post-event validation procedures that
694 ensure system accuracy and maintain stakeholder trust. The modular design of the system
695 allows it to be adapted to various regional monitoring networks and institutional frameworks,
696 making it versatile and scalable across different geographic and organizational contexts.

697 **6.4 Limitations and future research directions**

698 Despite promising advancements, this study has limitations owing to the complexity of
699 typhoon-induced landslides. First, the model's validation relies solely on landslides from
700 Typhoon Gaemi. While this single event provided a comprehensive dataset, validating against
701 multiple, varied typhoons is crucial for model robustness. Typhoons differ significantly in
702 intensity, rainfall patterns, forward speed, and seasonality, all of which can influence
703 threshold parameters. For instance, a slow-moving typhoon with higher cumulative rainfall
704 and lower peak intensity could alter the optimal H24-D7 ratios. Future research should
705 incorporate landslide inventories from typhoons with contrasting characteristics to assess
706 threshold transferability and develop adaptive parameterization. The framework's modular
707 design readily facilitates this by allowing recalibration of the RC24 coefficient for different
708 typhoon types.

709 Second, the current study primarily addresses rainfall-induced landslides, overlooking
710 other potential contributing factors. Future work should explore integrating multiple
711 triggering mechanisms, including earthquakes, human-induced slope modifications, and
712 typhoon rainfall, for a more comprehensive hazard assessment.

713 Third, the study doesn't explicitly address the potential impacts of climate change on
714 typhoon rainfall and landslide occurrence. As climate change alters typhoon frequency,

刪除[肖巍峰]: The integration of landslide susceptibility maps with spatially distributed rainfall thresholds resulted in a comprehensive hazard warning system for Zixing City. This approach, combining spatial probability (LSP) and temporal probability (rainfall thresholds), addresses the limitations ()

刪除[肖巍峰]: 5

715 intensity, and tracks, future studies should incorporate climate projections specific to
716 typhoon-prone regions. This will enable the development of forward-looking landslide
717 warning systems that can adapt to the evolving threats posed by typhoon-specific rainfall.

718 Fourth, while this study demonstrates the effectiveness of ML approaches, further
719 refinement is possible. Future research should explore advanced deep learning techniques and
720 ensemble methods to better capture the complex, non-linear relationships between typhoon-
721 related variables (e.g., rainfall intensity, duration, antecedent moisture) and slope stability.
722 These advanced methods may offer improved predictive accuracy, more robust uncertainty
723 quantification, and ultimately, more reliable hazard warnings.

724 Finally, climate projections for Southeast China show a 15–25% increase in peak
725 typhoon rainfall by 2080 (RCP8.5), which could alter the H24–D7 landslide thresholds from
726 this study. Higher atmospheric moisture may lower D7 thresholds, while greater rainfall
727 intensity could require new H24 parameters. Shifting typhoon tracks and seasonality might
728 also change which areas are vulnerable. Future work must use downscaled climate data to
729 create non-stationary thresholds, ensuring the long-term reliability of warning systems in the
730 region.

71 7 Conclusions

731 This study establishes a novel integrated framework combining optimized LSP with
732 typhoon-specific rainfall threshold modeling for comprehensive hazard assessment in
733 mountainous regions. Through systematic analysis of 705 landslides triggered by Typhoon
734 Gaemi in Zixing City, several key insights emerge:

735 (1) Buffer distance optimization proves critical for typhoon-induced landslide modeling,
736 with SVM-FR combinations at 0.5–2.0 km distances achieving superior performance (F1-
737 score: 0.859) compared to conventional approaches. This spatial scale effectively captures

删除[肖巍峰]: Despite the significant advancements made in this study, several limitations exist, especially when considering the complex and dynamic nature of typhoon - induced landslides. Firstly, the model validation predominantly depends on a single landslide event trigger...
...

删除[肖巍峰]: This study presents an integrated framework for optimizing landslide susceptibility prediction and rainfall threshold modeling to develop a comprehensive hazard warning system for Zixing City, China. The key conclusions are as follows:

739 typhoon-induced moisture infiltration patterns that differ fundamentally from other triggering
740 mechanisms.

741 (2) The H24-D7 threshold model demonstrates exceptional stability (71.8% accuracy
742 across 5-fold validation), successfully characterizing the dual-phase failure mechanism unique
743 to typhoons: prolonged antecedent saturation coupled with intense precipitation bursts during
744 typhoon passage.

745 (3) Spatially distributed rainfall thresholds reveal significant heterogeneity, reflecting
746 complex interactions between typhoon structure and local topography that contradict uniform
747 regional threshold assumptions in existing operational systems.

748 (4) The integrated warning system achieves operational efficiency through dual-
749 threshold configuration: H24 thresholds provide immediate response capability during
750 typhoon landfall, while D7 thresholds enable early detection of vulnerable areas approaching
751 saturation conditions.

752 (5) This framework addresses three critical gaps in current landslide prediction:
753 systematic buffer optimization for imbalanced datasets, effective integration of variable
754 weighting with machine learning algorithms, and development of typhoon-specific spatially
755 explicit thresholds.

756
757
758
759 *Code and data availability.* The source code and data will be made available on request.

760 *Competing interests.* The contact author has declared that none of the authors has any
761 competing interests.

762 *Author contributions.* **Weifeng Xiao:** Writing-review & editing, Validation,
763 Conceptualization. **Guangchong Yao:** Visualization, Validation, Data curation. **Zhenghui**
764 **Xiao:** Writing-review & editing, Formal analysis. **Ge Liu:** Resource, Correspondence.

删除[肖巍峰]: The comparative analysis of SVM and LightGBM models revealed that SVM with FR input at 0.5 km and 2.0 km buffer distances achieved optimal performance in landslide susceptibility prediction. This highlights the importance of careful consideration of spatial scale and input variable selection in susceptibility modeling.

The H24-D7 model, integrating 24-hour typhoon rainfall bursts and 7-day antecedent moisture—key components of typhoon hydrology—achieved the highest accuracy (71.8%), revealing how typhoon-induced saturation and intense rainfall synergistically drive slope failure.

The typhoon-adapted hazard warning system, merging susceptibility maps with dynamic rainfall thresholds, showed 71.4% overlap with historical landslides, confirming the utility of linking spatial slope vulnerability to typhoon rainfall patterns.

The 24-hour and 7-day warning maps unveiled divergent failure mechanisms: short-term typhoon downpours triggering abrupt slope failures vs. prolonged antecedent rainfall inducing gradual soil saturation, underscoring the need for temporally explicit hazard assessments.

The developed framework demonstrates significant potential for improving landslide risk management by providing spatially explicit hazard warnings that account for both inherent susceptibility and dynamic rainfall conditions.

765 **Luguang Luo**: Visualization, Validation, Investigation, Data curation. **Yunjiang Cao**:
766 Visualization, Formal analysis, Data curation. **Wei Yin**: Validation, Investigation.
767 *Acknowledgments.* This research was funded by the Research Project on Natural Resources of
768 Hunan Provincial Department of Natural Resources (No. HBZ20240112), the Open Research
769 Topic of Hunan Geological Disaster Monitoring Early Warning and Emergency Rescue
770 Engineering Technology Research Center (No. hndzgczx202409), and the Hunan Provincial
771 Natural Science Foundation of China (No. 2023JJ30238).

772

773

774

775 **References**

776 Achu, A. L., Aju, C. D., Pham, Q. B., Reghunath, R., and Anh, D. T.: Landslide susceptibility modeling
777 using hybrid bivariate statistical - based machine - learning method in a highland segment of Southern
778 Western Ghats, India, *Environ. Earth Sci.*, 81, 361, <https://doi.org/10.1007/s12665-022-10464-z>, 2022.

779 **Banfi, F. and De Michele, C.: Temporal clustering of precipitation driving landslides over the Italian**
780 **Territory, Earths Future, 12, e2023EF003885, https://doi.org/10.1029/2023EF003885, 2024.**

781 **Bogaard, T. and Greco, R.: Hydrological perspectives on precipitation intensity-duration thresholds for**
782 **landslide initiation: proposing hydro-meteorological thresholds, Nat. Hazards Earth Syst. Sci., 18, 31–39,**
783 <https://doi.org/10.5194/nhess-18-31-2018>, 2018.

784 **Calvello, M. and Piciullo, L.: Assessing the performance of regional landslide early warning models: the**
785 **EDuMaP method, Nat. Hazards Earth Syst. Sci., 16, 103–122, https://doi.org/10.5194/nhess-16-103-**
786 **2016, 2016.**

787 **Chang, Z. L., Huang, J. S., Huang, F. M., Bhuyan, K., Meena, S. R., and Catani, F.: Uncertainty analysis of**
788 **non-landslide sample selection in landslide susceptibility prediction using slope unit-based machine**
789 **learning models, Gondwana Res., 117, 307–320, https://doi.org/10.1016/j.gr.2023.02.007, 2023.**

790 Cho, W., Park, J., Moon, J., Cha, D. H., Moon, Y. M., Kim, H. S., Noh, K. J., and Park, S. H.: Effects of
791 topography and sea surface temperature anomalies on heavy rainfall induced by Typhoon Chaba in 2016,
792 *Geosci. Lett.*, 9, 29, <https://doi.org/10.1186/s40562-022-00230-1>, 2022.

793 Chung, C. C. and Li, Z. Y.: Rapid landslide risk zoning toward multi-slope units of the Neikuihui tribe for
794 preliminary disaster management, *Nat. Hazards Earth Syst. Sci.*, 22, 1777–1794,
795 <https://doi.org/10.5194/nhess-22-1777-2022>, 2022.

796 Ciurleo, M., Cascini, L., and Calvello, M.: A comparison of statistical and deterministic methods for
797 shallow landslide susceptibility zoning in clayey soils, *Eng. Geol.*, 223, 71–81,
798 <https://doi.org/10.1016/j.enggeo.2017.04.023>, 2017.

799 Dou, H. Q., He, J. B., Huang, S. Y., Jian, W. B., and Guo, C. X.: Influences of non - landslide sample
800 selection strategies on landslide susceptibility mapping by machine learning, *Geomat. Nat. Haz. Risk*, 14,
801 1–15, <https://doi.org/10.1080/19475705.2023.2285719>, 2023.

802 Fan, W., Wei, X. S., Cao, Y. B., and Zheng, B.: Landslide susceptibility assessment using the certainty
803 factor and analytic hierarchy process, *J. Mt. Sci.*, 14, 906–925, <https://doi.org/10.1007/s11629-016-4068-2>, 2017.

804 Fan, W., Wei, Y. N., and Deng, L. S.: Failure modes and mechanisms of shallow debris landslides using an
805 artificial rainfall model experiment on Qin-ba Mountain, *Int. J. Geomech.*, 18, 04017157,
806 [https://doi.org/10.1061/\(ASCE\)GM.1943 - 5622.0001068](https://doi.org/10.1061/(ASCE)GM.1943 - 5622.0001068), 2018.

807 Froude, M. J., and Petley, D. N.: Global fatal landslide occurrence from 2004 to 2016, *Nat. Hazards Earth
808 Syst. Sci.*, 18, 2161–2181, <https://doi.org/10.5194/nhess - 18 - 2161 - 2018>, 2018.

809 Gariano, S. L., Brunetti, M. T., Iovine, G., Melillo, M., Peruccacci, S., Terranova, O., Vennari, C., and
810 Guzzetti, F.: Calibration and validation of rainfall thresholds for shallow landslide forecasting in Sicily,
811 southern Italy, *Geomorphology*, 228, 653–665, <https://doi.org/10.1016/j.geomorph.2014.10.019>, 2015.

812 Gariano, S. L., and Guzzetti, F.: Landslides in a changing climate, *Earth - Sci. Rev.*, 162, 227–252,
813 <https://doi.org/10.1016/j.earscirev.2016.08.011>, 2016.

814 Guo, W. X., Ye, J., Liu, C. B., Lv, Y. J., Zeng, Q. Y., and Huang, X.: An approach for predicting landslide
815 susceptibility and evaluating predisposing factors, *Int. J. Appl. Earth Obs.*, 135, 104217,
816 <https://doi.org/10.1016/j.jag.2024.104217>, 2024.

删除[肖巍峰]: Caine, N.: The rainfall intensity: duration
control of shallow landslides and debris flows, *Geog. Ann. A.*,
62, 23–27, <https://doi.org/10.2307/520449>, 1980.
Chang, Z. L., Huang, J. S., Huang, F. M., Bhuyan, K., Meena,
S. R., and Catani, F.: Uncertainty analysis of non - landslide
sample selection in landslide susceptibility prediction using
slope unit - based machine learning models, *Gondwana Res.*,
117, 307–320, <https://doi.org/10.1016/j.gr.2023.02.007>, 2023.
Chen, W., Pourghasemi, H. R., and Zhao, Z.: A GIS - based
comparative study of Dempster - Shafer, logistic regression
and artificial neural network models for landslide
susceptibility mapping, *Geocarto Int.*, 32, 367–385,
<https://doi.org/10.1080/10106049.2016.1140824>, 2017.
Chen, W., Xie, X. S., Wang, J. L., Pradhan, B., Hong, H. Y.,
Bui, D. T., Duan, Z., and Ma, J. Q.: A comparative study of
logistic model tree, random forest, and classification and
regression tree models for spatial prediction of landslide
susceptibility, *Catena*, 151, 147–160,
<https://doi.org/10.1016/j.catena.2016.11.032>, 2017.

818 Guzzetti, F., Gariano, S. L., Peruccacci, S., Brunetti, M. T., Marchesini, I., Rossi, M., and Melillo, M.:
819 Geographical landslide early warning systems, *Earth - Sci. Rev.*, 200, 102973,
820 <https://doi.org/10.1016/j.earscirev.2019.102973>, 2020.

821 Guzzetti, F.: Invited perspectives: Landslide populations - can they be predicted?, *Nat. Hazards Earth Syst.*
822 *Sci.*, 21, 1467–1471, <https://doi.org/10.5194/nhess-21-1467-2021>, 2021.

823 Huang, F., Cao, Z. S., Guo, J. F., Jiang, S. H., Li, S., and Guo, Z. Z.: Comparisons of heuristic, general
824 statistical and machine learning models for landslide susceptibility prediction and mapping, *Catena*, 191,
825 104580, <https://doi.org/10.1016/j.catena.2020.104580>, 2020.

826 Huang, F., Cao, Y., Li, W., Catani, F., Song, G., Huang, J., and Yu, C.: Uncertainties of landslide
827 susceptibility prediction: influences of different study area scales and mapping unit scales, *Int. J. Coal*
828 *Sci. Technol.*, 11, 26, <https://doi.org/10.1007/s40789-024-00678-w>, 2024.

829 Huang, F., Chen, J., Liu, W., Huang, J., Hong, H., and Chen, W.: Regional rainfall - induced landslide
830 hazard warning based on landslide susceptibility mapping and a critical rainfall threshold,
831 *Geomorphology*, 408, 108236, <https://doi.org/10.1016/j.geomorph.2022.108236>, 2022.

832 Huang, Y., and Zhao, L.: Review on landslide susceptibility mapping using support vector machines,
833 *Catena*, 165, 520–529, <https://doi.org/10.1016/j.catena.2018.03.003>, 2018.

834 Kalantar, B., Pradhan, B., Naghibi, S. A., Motevalli, A., and Mansor, S.: Assessment of the effects of
835 training data selection on the landslide susceptibility mapping: A comparison between support vector
836 machine (SVM), logistic regression (LR), and artificial neural networks (ANN), *Geomat. Nat. Haz. Risk*,
837 9, 49–69, <https://doi.org/10.1080/19475705.2017.1407368>, 2018.

838 Kenanoglu, M. B., Ahmadi - Adli, M., Toker, N. K., and Huvaj, N.: Effect of unsaturated soil properties on
839 the intensity - duration threshold for rainfall triggered landslides, *Tek. Dergi*, 30, 9009–9027,
840 <https://doi.org/10.18400/tekderg.414884>, 2019.

841 [Kirschbaum, D. and Stanley, T.: Satellite-Based Assessment of Rainfall-Triggered Landslide Hazard for](#)
842 [Situational Awareness, *Earth's Future*, 6, 505–523, <https://doi.org/10.1002/2017EF000715>, 2018.](#)

843 [Lee, J. T., Ko, K. Y., Lee, D. I., You, C. H., and Liou, Y. C.: Enhancement of orographic precipitation in](#)
844 [Jeju Island during the passage of Typhoon Khanun \(2012\), *Atmos. Res.*, 201, 58–71,](#)
845 <https://doi.org/10.1016/j.atmosres.2017.10.013>, 2018.

846 Li, Y. L., Lin, Y. L., and Wang, Y. Q.: A Numerical Study on the Formation and Maintenance of a Long -
847 Lived Rainband in Typhoon Longwang (2005), *J. Geophys. Res. Atmos.*, 124(19), 10401–10426,
848 <https://doi.org/10.1029/2019JD030600>, 2019.

849 Liu, L. L., Zhang, Y. L., Xiao, T., and Yang, C.: A frequency ratio - based sampling strategy for landslide
850 susceptibility assessment, *Bull. Eng. Geol. Environ.*, 81, 360, <https://doi.org/10.1007/s10064-022-02836-3>, 2022.

851
852 [Liu, M. F., Vecchi, G. A., Smith, J. A., and Murakami, H.: The present-day simulation and Twenty-First-](#)
853 [Century Projection of the Climatology of Extratropical Transition in the North Atlantic, *J. Climate*, 30,](#)
854 [2739–2756, https://doi.org/10.1175/JCLI-D-16-0352.1, 2017.](#)

855 Lombardo, L., and Mai, P. M.: Presenting logistic regression - based landslide susceptibility results, *Eng.*
856 *Geol.*, 244, 14–24, <https://doi.org/10.1016/j.enggeo.2018.07.019>, 2018.

857
858 [Ma, H., Wang, F. W., Fu, Z. J., Feng, Y. Q., You, Q., and Li, S.: Characterizing the clustered landslides](#)
859 [triggered by extreme rainfall during the 2024 typhoon Gaemi in Zixing City, Hunan Province, China,](#)
860 [*Landslides*, 22, 2311–2329, https://doi.org/10.1007/s10346-025-02510-1, 2025.](#)

861 Merghadi, A., Yunus, A. P., Dou, J., Whiteley, J., ThaiPham, B., Bui, D. T., Avtar, R., and Abderrahmane,
862 B.: Machine learning methods for landslide susceptibility studies: A comparative overview of algorithm
863 performance, *Earth-Sci. Rev.*, 207, 103225, <https://doi.org/10.1016/j.earscirev.2020.103225>, 2020.

864 Mirus, B. B., Becker, R. E., Baum, R. L., and Smith, J. B.: Integrating real - time subsurface hydrologic
865 monitoring with empirical rainfall thresholds to improve landslide early warning, *Landslides*, 15, 1909–
866 1919, <https://doi.org/10.1007/s10346-018-0995-z>, 2018.

867 Mondini, A. C., Guzzetti, F., and Melillo, M.: Deep learning forecast of rainfall - induced shallow
868 landslides, *Nat. Commun.*, 14, 10.1038/s41467-023-38135-y, <https://doi.org/10.1038/s41467-023-38135-y>, 2023.

870 Niu, H. T., Shao, S. J., Gao, J. Q., and Jing, H.: Research on GIS-based information value model for
871 landslide geological hazards prediction in soil - rock contact zone in southern Shaanxi, *Phys. Chem.*
872 *Earth*, 133, 103515, <https://doi.org/10.1016/j.pce.2023.103515>, 2024.

删除[肖巍峰]: Long, K., Zhang, S. J., Wei, F. Q., Hu, K. H.,
Zhang, Q., and Luo, Y.: A hydrology - process based method
for correlating debris flow density to rainfall parameters and
its application on debris flow prediction, *J. Hydrol.*, 589,
125124, <https://doi.org/10.1016/j.jhydrol.2020.125124>, 2020.
Lv, L., Chen, T., Dou, J., and Plaza, A.: A hybrid ensemble -
based deep - learning framework for landslide susceptibility
mapping, *Int. J. Appl. Earth Obs.*, 108, 102713,
<https://doi.org/10.1016/j.jag.2022.102713>, 2022.
Marra, F.: Rainfall thresholds for landslide occurrence:
systematic underestimation using coarse temporal resolution
data, *Nat. Hazards*, 95, 883–890,
<https://doi.org/10.1007/s11069-018-3508-4>, 2019.

873 [Nocentini, N., Medici, C., Barbadori, F., Gatto, A., Franceschini, R., del Soldato, M., Rosi, A., and Segoni,](#)
874 [Optimization of rainfall thresholds for landslide early warning through false alarm reduction and a](#)
875 [multi-source validation, Landslides, 21, 557–571, <https://doi.org/10.1007/s10346-023-02176-7>, 2024.](#)

876 [Nolasco-Javier, D. and Kumar, L.: Deriving the rainfall threshold for shallow landslide early warning](#)
877 [during tropical cyclones: a case study in northern Philippines, Nat. Hazards, 90, 921–941,](#)
878 [https://doi.org/10.1007/s11069-017-3081-2, 2018.](https://doi.org/10.1007/s11069-017-3081-2)

879 Panchal, S., and Shrivastava, A. K.: A comparative study of frequency ratio, Shannon's entropy and
880 analytic hierarchy process (AHP) models for landslide susceptibility assessment, ISPRS Int. J. Geo-Inf.,
881 10, 603, <https://doi.org/10.3390/ijgi10090603>, 2021.

882 Piciullo, L., Calvello, M., and Cepeda, J. M.: Territorial early warning systems for rainfall - induced
883 landslides, Earth-Sci. Rev., 179, 228–247, <https://doi.org/10.1016/j.earscirev.2018.02.013>, 2018.

884 Piciullo, L., Gariano, S. L., Melillo, M., Brunetti, M. T., Peruccacci, S., Guzzetti, F., and Calvello, M.:
885 Definition and performance of a threshold - based regional early warning model for rainfall - induced
886 landslides, Landslides, 14, 995–1008, <https://doi.org/10.1007/s10346-016-0750-2>, 2017.

887 Pourghasemi, H. R., and Rahmati, O.: Prediction of the landslide susceptibility: Which algorithm, which
888 precision?, Catena, 162, 177–192, <https://doi.org/10.1016/j.catena.2017.11.022>, 2018.

889 Regmi, N. R., Walter, J. I., Jiang, J. L., Orban, A. M., and Hayman, N. W.: Spatial patterns of landslides in
890 a modest topography of the Ozark and Ouachita Mountains, USA, Catena, 245, 108344,
891 <https://doi.org/10.1016/j.catena.2024.108344>, 2024.

892 Reichenbach, P., Rossi, M., Malamud, B. D., Mihir, M., and Guzzetti, F.: A review of statistically - based
893 landslide susceptibility models, Earth-Sci. Rev., 180, 60–91,
894 <https://doi.org/10.1016/j.earscirev.2018.03.001>, 2018.

895 Sahin, E. K.: Comparative analysis of gradient boosting algorithms for landslide susceptibility mapping,
896 Geocarto Int., 37, 2441–2465, <https://doi.org/10.1080/10106049.2020.1831623>, 2022.

897 San, B. T.: An evaluation of SVM using polygon-based random sampling in landslide susceptibility
898 mapping: The Candir catchment area (western Antalya, Turkey), Int. J. Appl. Earth Obs., 26, 399–412,
899 <https://doi.org/10.1016/j.jag.2013.09.010>, 2014.

900 Segoni, S., Lagomarsino, D., Fanti, R., Moretti, S., and Casagli, N.: Integration of rainfall thresholds and
901 susceptibility maps in the Emilia Romagna (Italy) regional - scale landslide warning system, *Landslides*,
902 12, 773–785, <https://doi.org/10.1007/s10346-014-0502-0>, 2015.

903 Segoni, S., Piciullo, L., and Gariano, S. L.: A review of the recent literature on rainfall thresholds for
904 landslide occurrence, *Landslides*, 15, 1483–1501, <https://doi.org/10.1007/s10346-018-0966-4>, 2018.

905 Segoni, S., Rosi, A., Lagomarsino, D., Fanti, R., and Casagli, N.: Brief communication: Using averaged
906 soil moisture estimates to improve the performances of a regional - scale landslide early warning system,
907 *Nat. Hazards Earth Syst. Sci.*, 18, 807–812, <https://doi.org/10.5194/nhess-18-807-2018>, 2018.

908 Sharma, L. P., Patel, N., Ghose, M. K., and Debnath, P.: Development and application of Shannon's
909 entropy integrated information value model for landslide susceptibility assessment and zonation in
910 Sikkim Himalayas in India, *Nat. Hazards*, 75, 1555–1576, <https://doi.org/10.1007/s11069-014-1378-y>,
911 2015.

912 Steger, S., Brenning, A., Bell, R., and Glade, T.: The propagation of inventory - based positional errors into
913 statistical landslide susceptibility models, *Nat. Hazards Earth Syst. Sci.*, 16, 2729–2745,
914 <https://doi.org/10.5194/nhess-16-2729-2016>, 2016.

915 Sun, D. L., Wu, X. Q., Wen, H. J., and Gu, Q. Y.: A LightGBM-based landslide susceptibility model
916 considering the uncertainty of non-landslide samples, *Geomat. Nat. Haz. Risk*, 14, 2213807,
917 <https://doi.org/10.1080/19475705.2023.2213807>, 2023.

918 [Sun, Y., Zhang, J., Wang, H. A., and Lu, D. G.: Probabilistic thresholds for regional rainfall induced](#)
919 [landslides, Comput. Geotech.](#), 166, 106040, <https://doi.org/10.1016/j.compgeo.2023.106040>, 2024.

920 Thiene, M., Shaw, W. D., and Scarpa, R.: Perceived risks of mountain landslides in Italy: Stated choices for
921 subjective risk reductions, *Landslides*, 14, 1077–1089, <https://doi.org/10.1007/s10346-016-0741-3>, 2017.

922 Tufano, R., Formetta, G., Calcaterra, D., and De Vita, P.: Hydrological control of soil thickness spatial
923 variability on the initiation of rainfall-induced shallow landslides using a three - dimensional model,
924 *Landslides*, 18, 3367–3380, <https://doi.org/10.1007/s10346-021-01681 - x>, 2021.

925 [Xiao, W. F., Zhou, Z. Y., Ren, B. Z., and Deng, X. P.: Integrating spatial clustering and multi - source](#)
926 [geospatial data for comprehensive geological hazard modeling in Hunan Province, Sci. Rep.](#), 15, 1982,
927 <https://doi.org/10.1038/s41598-024-84825 - y>, 2025.

删除[肖巍峰]: Wang, H. J., Zhang, L. M., Yin, K. S., Luo, H. Y., and Li, J. H.: Landslide identification using machine learning, *Geosci. Front.*, 12(1), 351–364, <https://doi.org/10.1016/j.gsf.2020.02.012>, 2021.

928 Yan, F., Zhang, Q. W., Ye, S., and Ren, B.: A novel hybrid approach for landslide susceptibility mapping
929 integrating analytical hierarchy process and normalized frequency ratio methods with the cloud model,
930 *Geomorphology*, 327, 170–187, <https://doi.org/10.1016/j.geomorph.2018.10.024>, 2019.

931 Yang, C., Liu, L. L., Huang, F. M., Huang, L., and Wang, X. M.: Machine learning - based landslide
932 susceptibility assessment with optimized ratio of landslide to non-landslide samples, *Gondwana Res.*,
933 123, 198–216, <https://doi.org/10.1016/j.gr.2022.05.012>, 2023.

934 Yang, K. H., Uzuoka, R., Thu, J. N., Lin, G. L., and Nakai, Y.: Coupled hydro-mechanical analysis of two
935 unstable unsaturated slopes subject to rainfall infiltration, *Eng. Geol.*, 216, 13–30,
936 <https://doi.org/10.1016/j.enggeo.2016.11.006>, 2017.

937 Zêzere, J. L., Pereira, S., Melo, R., Oliveira, S. C., and Garcia, R. A. C.: Mapping landslide susceptibility
938 using data-driven methods, *Sci. Total Environ.*, 589, 250–267,
939 <https://doi.org/10.1016/j.scitotenv.2017.02.188>, 2017.

940 Zhao, Z., Liu, Z. Y., and Xu, C.: Slope unit-based landslide susceptibility mapping using certainty factor,
941 support vector machine, random forest, CF-SVM and CF-RF models, *Front. Earth Sci.*, 9, 589630,
942 <https://doi.org/10.3389/feart.2021.589630>, 2021.

943 Zou, Y., Wei, Z. F., Zhan, Q. M., and Zhou, H. J.: An extreme storm over the Nanling Mountains during
944 Typhoon Bilis and the roles of terrain, *Nat. Hazards*, 116, 795–815, <https://doi.org/10.1007/s11069-022-05699-9>, 2023.

删除[肖巍峰]: Zhang, W. A., Gu, X., Tang, L. B., Yin, Y. P.,
Liu, D. S., and Zhang, Y. M.: Application of machine learning,
deep learning and optimization algorithms in geoengineering
and geoscience: Comprehensive review and future challenge,
Gondwana Res., 109, 1–17,
<https://doi.org/10.1016/j.gr.2022.03.015>, 2022.